Molecular Nanomagnets for Novel Spintronics Devices

by

Sean Walker

A thesis
presented to the University of Waterloo
in fulfilment of the
thesis requirement for the degree of
Master of Science
in
Chemistry - Quantum Information

Waterloo, Ontario, Canada, 2016

Author's Declaration

I hereby declare that I am the sole author of this thesis. This is a true copy of the thesis, including any required final revisions, as accepted by my examiners.

I understand that my thesis may be made electronically available to the public.

Abstract

Molecular nanomagnets possess interesting quantum properties that make them potential candidates for qubits in quantum information processing. Heterometallic antiferromagnetic wheels specifically have been shown to have a coherence time long enough to permit quantum computing operations. The field of molecular spintronics deals with the integration of molecular nanomagnets into nanoelectronic devices for the purpose of probing and manipulating these quantum properties. In order for a nanomagnet to be incorporated into such a device it needs to be both magnetically and structurally stable when in contact with nanoelectronic components, and its coupling to the environment needs to be controlled.

The first part of this thesis deals with the synthesis and characterization of a derivative of a member of the Cr_7Ni family of heterometallic antiferromagnetic wheels. The synthetic process involved introducing long alkyl chains into the organic shell of the nanomagnet in order that it may interact with carbon-based nanoelectronic devices in a non-destructive capacity. The molecule was characterized in order to confirm the results of the synthesis, to gain a greater understanding of how its magnetic properties can be modelled, and to fingerprint the system in order to acquire data that will help determine whether its properties remain intact when attached to a graphene surface.

The second part of this thesis concerns a series of experiments conducted toward developing a process for determining the viability of the synthesized nanomagnet as the molecular component in spintronics devices. To begin to determine the molecule's magnetic and structural stability when deposited on a graphene surface the first step is to realize clean graphene substrates that are suitably pristine such that a nanometre sized particle can be detected. Graphene flakes were fabricated using the mechanical exfoliation technique and a procedure was developed for cleaning the resulting flakes of residues. The next step of this research will consist of conducting systematic studies to quantify the binding affinity of the nanomagnet species to both graphene and to pristine carbon nanotubes, and to determine whether the system retains its structural and magnetic properties when attached to graphitic surfaces. The work described here lays the foundation for the novel use of Cr_7Ni-eth and other functionalized magnetic molecules in spin-based nanoelectronic devices.

Acknowledgements

I would like to acknowledge all of the support I have received from many sources during my Masters studies. Firstly, I would like to thank my supervisor Jonathan Baugh for his guidance and encouragement. I look forward to continuing my research with him as a PhD student.

All of the members, past and present, of the Baugh research group have made graduate studies enjoyable; I would like to thank Greg, Kaveh, Kyle, Chris, Brandon, Franklin, Mitchell, and Eduardo for all their help.

I would also like to thank Cameron for all his hard work and expertise regarding graphene exfoliations.

I am appreciative of the members of my committee, Dr. Shirley Tang and Dr. Guoxing Miao. I would like to especially thank Dr. Shirley Tang for allowing me to conduct portions of this research in her laboratory. Members of the Tang research group: Zhi, for helping me with Raman and AFM, and for his time spent working with graphene oxide; Louis for always letting me into the lab and for many helpful suggestions.

I am also very appreciative of Dr. Nan Chen and Dr. Anthony Krismanich for numerous invaluable discussions, and providing thorough explanations related to various aspects of this research.

I would lastly like to thank Dr. Howard Siu for allowing me access to the FTIR spectrometer and training me on the instrument.

This work was funded in part by the support of NSERC and the Waterloo Institute for Nanotechnology.

Contents

List of Figures

List of Tables

List of Abbreviations

AFW	Antiferromagnetic wheels
$Cr_7Mn-piv$	$[H_2(CH_3CH_2)_2N][Cr_7MnF_8(O_2CC(CH_3)_3)_{16}]$, an example of a heterometallic ring.
$Cr_7Ni-eth(p)$	The Cr_7Ni derivative synthesized with dipropylamine.
$Cr_7Ni-eth$	$[(CH_3CH_2)_2NH_2][Cr_7NiF_8(C_8H_{16}O_2)_{16}]$, a Cr_7Ni derivative
Cr_7Ni	The SMM family with the general formula $[H_2R_2N][Cr_7NiF_8(O_2CCR')_{16}]$
Cr_8-piv	The homometallic ring $Cr_8F_8(O_2CC(CH_3)_3)_{16}$
$Mn_{12}-acetate$	The SMM $Mn_{12}O_{12}(CH_3COO)_{16}(H_2O)_4$
Mn_3-anth	The anthracene substituted species of the Mn_3 SMM
Mn_3-naph	The naphthalene substituted species of the Mn_3 SMM
Mn_3-pyr	The pyrene substituted species of the Mn_3 SMM
MN	Molecular nanomagnet
AFM	Atomic force microscopy
CNT	Carbon nanotube
CW-ESR	Continuous-wave electron spin resonance
FTIR	Fourier transform infrared spectroscopy
FWHM	Full width at half maximum
GO	Graphene oxide

GSA	Giant spin approximation
MAPLE	Matrix-assisted pulsed laser evaporation
mpkoH	methyl 2-pyridyl ketone oxime
RMS	Root mean square
SMM	Single-molecule magnet
SQUID	Superconducting quantum interference device
STM	Scanning tunnelling microscopy
TLC	Thin layer chromatography
UV-Vis	Ultraviolet-visible spectroscopy
XAS	X-ray absorption spectroscopy
XMCD	X-ray magnetic circular dichroism
XPS	X-ray photoelectron spectroscopy
XRD	X-ray diffraction

Chapter 1

Introduction

As technology shrinks ever smaller in dimension, the search for materials that exhibit potentially useful and novel properties intensifies. One consequence of the reduced size of these emerging materials, whose dimensions are often on the nanometre scale, is that quantum phenomena become increasingly relevant when considering their applications. Rather than posing a limitation to technological growth, these phenomena can in fact be uniquely exploited to create devices that actually outperform existing technologies [62, 31]. The experimental realization of these devices not only presents a significant engineering undertaking, but also serves as a platform for probing the laws of physics. Many systems exist that are worthy of study solely because of their potential for revealing interesting quantum properties. Numerous questions remain regarding the foundations of quantum mechanics, and gaining greater insight into the unique properties exhibited by different materials is valuable from both a theoretical perspective, and in terms of guiding research towards conquering the engineering challenges inherent to modern technological applications.

Quantum computing represents one such exciting platform for experimentation [54]. Despite the promise demonstrated by numerous theoretical results in quantum information processing, there remain several fundamental questions that need to be addressed concerning the experimental realization of a quantum computer. Even the physical form a quantum computer will eventually take is still an open question with numerous quantum systems being proposed as potential qubits [16, 48, 17, 36]. Several proposals involve controlling the magnetic degrees of freedom within a molecular system, focussing on harnessing both the nuclear spins associated with certain molecules [29], as well as the electronic spins [43]. These proposals encompass a wide range of scientific fields, from semiconductor physics [48] to nuclear magnetic resonance [29]. By pursuing the realization of a quantum computer borne out of the magnetic properties of materials, scientists have managed to probe even deeper into the fundamental laws of spin physics.

In general, magnetic materials have not been immune to the miniaturization of technology. Molecular nanomagnets represent the logical continuation of this miniaturization [28]. A nanomagnet is a magnetic system whose physical dimensions are

on the nanometre scale, and which exhibits properties similar to a ferromagnet. Like a ferromagnet, a nanomagnet will have some magnetization even in the absence of an applied field. A molecular nanomagnet is a molecular system that behaves similarly to a nanomagnet, but whose magnetism originates on a molecular level [61]. Typically these systems will consist of a magnetic core of metal ions surrounded by organic ligands. The magnetic properties exhibited by the system depend on the core of the molecule, while the organic shell serves to both isolate the metal centres from intermolecular interactions and to facilitate the coupling of the system to its environment. Considering the magnetic core of a molecular nanomagnet is somewhat isolated, a crystalline sample of the molecule can be seen as a group of non-interacting, equivalent nanomagnets, and the magnetic properties of the total crystal can be approximated as that of a single instance of the molecule. Therefore, in a sense these systems exist at the boundary between the nanoscale and the macroscopic, displaying magnetic quantum phenomena common to the former while retaining the order and high degree of characterizability of the latter [23]. Molecular nanomagnets have garnered attention over the last two decades due to the interesting magnetic properties they exhibit, and because of their potential applications in both quantum memory storage and quantum computing [68, 43, 50, 74, 75, 81].

The utilization of molecular nanomagnets in technology is an example of a bottom-up approach to materials science. With the continued miniaturization of technology we are reaching the limit of the top-down fabrication strategy employed by the semiconductor industry [52]. Through lithographic techniques devices can be fabricated with feature sizes on the order of tens of nanometres, but there is still room for a greater degree of miniaturization to be attained. A bottom-up approach where technology is developed by combining molecular building blocks into functional nanostructures affords numerous advantages [5]. Most importantly, the properties of a molecule can be tailored using well-established methods of chemical synthesis. With the development of supramolecular chemistry, large, elaborate structures consisting of multiple interlocking components have been realized.

Rather than developing technology consisting solely of molecular building blocks, another approach involves integrating certain molecular components into devices. This method typically involves chemically modifying molecules that display interesting electronic or magnetic properties in a manner that will allow the molecule to interact with existing nanoelectronic technologies. Molecular spintronics is an example of such an approach, where molecular nanomagnets serve as the molecular components being incorporated into different devices [9, 26]. Depending on the geometry and nature of the device, the properties of molecular nanomagnets can be probed and manipulated [69, 77]. Although many of these systems present more of a scientific curiousity rather than a viable technological direction, this exploration of molecular magnetism offers a rich playground for the study of spin physics.

This thesis describes research toward the development of novel spintronics technologies. Most of the work focusses on determining whether a specific molecular nanomagnet, a heterometallic antiferromagnet wheel, is capable of being success-

fully integrated into a molecular spintronics device. In order for a molecular system to be viable for such an application it needs to be stable within the device geometry (i.e. retain its structural and magnetic properties) without compromising the performance of the nanoelectronic components. Determining whether a specific nanomagnet fits this criteria is a non-trivial task and as such much of the work performed was exploratory in nature. For example, the magnetic and structural properties of a synthesized molecular nanomagnet were characterized, in part, to simply gather information that would allow us to potentially interpret the results of future quantum transport experiments performed on a realized spintronics device.

This thesis is organized into four sections. Chapter 2 delves deeper into the field molecular nanomagnets , describing the magnetic properties that make these systems interesting to study. Two different types of magnetic systems will be presented: the typical single-molecule magnet characterized by a slow magnetic relaxation time and macroscopic tunneling of magnetic quantization, and antiferromagnetic heterometallic wheels.

In Chapter 3 the synthesis of a member of a family of antiferromagnetic wheels is discussed. After the general chemical structure and reactivity of this family is elaborated upon, more detail is given concerning the functionalization of a specific member of this family. Lastly, the different characterization tools employed for studying the product of the synthesis and the results of this characterization are presented.

Chapter 4 of this thesis describes electron spin resonance experiments conducted on molecular nanomagnets. The results of these experiments as well as attempts to simulate these results are given.

Lastly, in Chapter 5, a series of experiments dealing with quantifying the affinity of different molecular nanomagnets to adhere to graphene are discussed. Details are provided regarding what is required in order to be able to make a systematic comparison between how different molecular nanomagnets interact with graphene, and progress made in developing a process for studying the properties of molecular nanomagnets attached to graphene surfaces is highlighted.

Chapter 2

Molecular nanomagnets

Chapter 2 of this thesis introduces the field of molecular nanomagnets. After reviewing some fundamental concepts of magnetism, the magnetic characteristics of molecular nanomagnets are discussed, focussing on two categories of molecular systems: single-molecule magnets and antiferromagnetic wheels. Some of the unique properties exhibited by single-molecule magnets that have motivated progress in this field are then described, and the molecular system in which we are interested, the Cr_7Ni antiferromagnetic wheel, is introduced.

2.1 Introduction

There are several different forms of magnetism that differ based on the nature of the magnetic interactions they describe, as well as how they classify how the magnetic moments within a system will respond to an applied magnetic field. Other than diamagnetism all other forms of magnetic interactions involve the presence of unpaired electrons. In a paramagnetic material there are no interactions between unpaired electrons within the system, and in the presence of an external field, the magnetic moments of the unpaired electrons will tend to align with the direction of the applied field.

On the other hand, ferromagnetism, antiferromagnetism and ferrimagnetism are all characterized by a degree of magnetic ordering even in the absence of an external magnetic field. Ferromagnetism is the form of magnetism that gives rise to the existence of permanent magnets. In a ferromagnetic material, magnetic domains are formed, within which the unbalanced magnetic moments of the constituent electrons are aligned. Even in the absence of an external field a permanent, non-zero moment may exist within the total system due to the disproportionate sizes of the different domains. As an external field is applied, the domains that are aligned with the field will grow until eventually the material is magnetically saturated. Once the applied field is removed, a ferromagnet can retain its magnetization, i.e. have a magnetic memory, a property known as hysteresis that has been exploited in the

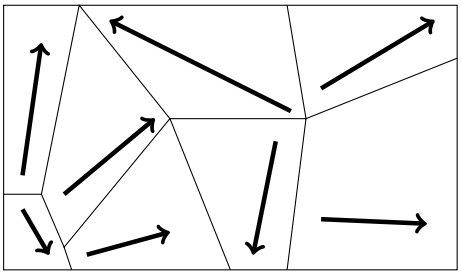

Figure 2.1: Magnetic domains in a bulk ferromagnetic material. In the presence of an external magnetic field the domains aligned with the applied field will grow until the system is magnetically saturated.

past in magnetic memory storage.

In an antiferromagnetic material adjacent magnetic moments will have the tendency to anti-align (i.e. point in opposite directions) causing a net magnetic moment of zero. This behaviour is typically only seen at low temperatures; above the Néel temperature associated with an antiferromagnetic system, the material will no longer exhibit the same magnetic interactions. Ferrimagnetism is similar to antiferromagnetism in that in a ferrimagnetic material adjacent magnetic moments will also tend to orient in an anti-parallel pattern. However, in a ferrimagnetic material, there exists an inherent imbalance in the opposing magnetic moments, causing a spontaneous magnetization at zero applied field.

A nanomagnet is a magnetic system whose size is submicronic that exhibits properties similar to that of a ferromagnet. Due to the small size of nanomagnets they do not form magnetic domains and thus can be seen as a single domain material. Such a magnetic system is limited by its superparamagnetic size, defined as the size at which the magnetic state of the system will fluctuate above a certain temperature. Common nanomagnets are typically grains of a bulk magnetic material such as iron. A molecular nanomagnet is a specific kind of nanomagnet whose magnetic properties originate on the molecular level.

We are interested in two varieties of molecular nanomagnets: single-molecule magnets and antiferromagnetic wheels. Single-molecule magnets (SMMs) are magnetic clusters that are categorized by a high-spin ground state and a large anisotropy, giving rise to slow magnetic relaxation below a certain temperature [61]. Antiferromagnetic wheels (AFWs) consist of a number of metal ions arranged in a ring where adjacent metal centres exhibit an antiferromagnetic exchange interaction. These magnetic clusters have attracted interest ever since it was proposed, and later shown, that such systems will display coherent oscillations of the Néel vector [51, 79].

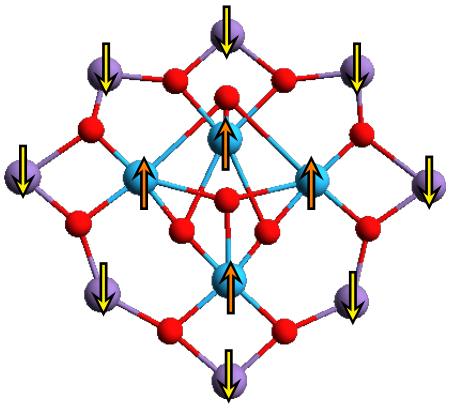

Figure 2.2: Schematic representation of the magnetic core of Mn_{12}−acetate. The total chemical formula of this SMM is $Mn_{12}O_{12}(CH_3COO)_{16}(H_2O)_4$. The Mn^{4+} (S = 3/2) and Mn^{3+} (S = 2) ions are antiferromagnetically coupled through a superexchange interaction mediated by the bridging oxygen atoms. In the above figure, the spins of the Mn centres are denoted by coloured arrows superimposed on each ion. This coupling leads to a high spin, $S = 10$ ground state. Atom colours: Mn^{4+}, blue; Mn^{4+}, purple; O, red.

2.2 Single-molecule magnets

The appearance of quantum phenomena in the classical world is uncommon. One example of such an occurrence occurs in the field of single-molecule magnetism, where macroscopic samples of SMMs have been shown to display quantum tunnelling of magnetization [22]. Mn_{12}−acetate, $Mn_{12}O_{12}(CH_3COO)_{16}(H_2O)_4$, synthesized by Lis (1980) [46], is the prototypical SMM; the structure of the molecule and its magnetic properties are representative of a wide variety of other SMMs. By illustrating how quantum tunnelling of magnetization arises out of the properties of Mn_{12}−acetate, one can gain greater insight into the magnetic mechanisms at work in these types of molecules.

2.2.1 Macroscopic quantum tunnelling of magnetization

The structure of Mn_{12}−acetate consists of a core of four Mn^{4+} ions (S = 3/2) arranged in a tetrahedral geometry, antiferromagnetically coupled to a ring of eight Mn^{3+} ions (S = 2) through bridging oxygen atoms (see Figure 2.2).[1] This antiferromagnetic coupling results in a high spin, S = 10 ground state [12]. A shell of acetate ligands encloses the magnetic interior. This general structure, comprised of a magnetic centre surrounded by organic ligands, is common to many species of SMMs.

[1] Avogadro: an open-source molecular builder and visualization tool (Version 1.1.1) was used throughout this thesis [32].

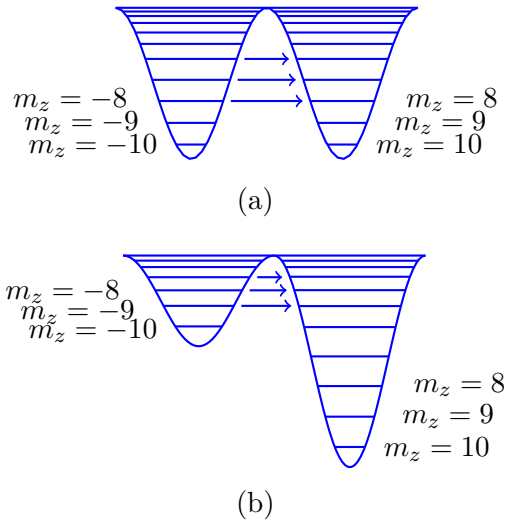

Figure 2.3: Bistable energy potential of $Mn_{12}-$acetate separated by anisotropic barrier. (a) With no external magnetic field. (b) An external field is applied along easy axis. By including terms in the spin Hamiltonian that do not commute with S_z, tunnelling between resonant energy levels is allowed at different values of the external magnetic field [23]. The arrows above indicate thermally assisted tunnelling processes.

The magnetic characteristics of the molecule are primarily determined by the inner core, while the outer shell can be chemically tuned to tailor other properties of the system.

The energy spectrum of $Mn_{12}-$acetate can be modelled as a double potential well where each well corresponds to either the spin-up or spin-down state of the molecule [61]. The $S = 10$ ground state of this SMM is characterized by a zero-field splitting of the different spin states $m_z = \pm 10, \pm 9, \ldots, \pm 1, 0$, and a large uniaxial anisotropic barrier that separates the two wells of the energy spectrum (Figure 2.3a). At low temperatures the spin state of $Mn_{12}-$acetate can be approximated using the following effective spin Hamiltonian:

$$\mathcal{H} \approx -DS_z^2 - g_z \mu_B S_z H_z - AS_z^4 + \mathcal{H}' \tag{2.1}$$

where S_z is the Pauli spin operator, μ_B is the Bohr magneton, H_z is the component of an applied static magnetic field in the z-direction, g_z is the g-factor, and A and D are parameters [23]. Given the high symmetry of this SMM, the first two terms are sufficient in describing the main features of the molecule's spin energy; the first term gives rise to the large anisotropic barrier that separates the two wells, while the second term represents the Zeeman energy that breaks the degeneracy of the spin-up and spin-down states in the presence of an applied magnetic field (Figure 2.3b)). As a result of the large anisotropic barrier, once an external field is applied initializing the system into either the spin-up or the spin-down state, and then removed, relaxation

of the magnetization of the SMM spin state will be very slow. Furthermore, even in the absence of an applied field, the SMM will have a non-zero magnetization. This behaviour will be observed as long as the thermal energy of the system is less than the anisotropic barrier. Consequently, at sufficiently low temperatures (for Mn_{12}-acetate approximately less than 4 K [61]), magnetic information can potentially be stored in the state of the molecule. By including additional higher order terms in the Hamiltonian (AS_z^4 in (2.1)) and terms that do not commute with S_z ($\mathcal{H}'$ in (2.1)), more defined structural features in the energy spectrum of the SMM can be elucidated, and quantum tunnelling of magnetization becomes allowed [6, 19].

Evidence for macroscopic tunnelling of magnetization can be seen in the hysteresis curve of $Mn_{12}-$acetate measured below the blocking temperature of the SMM [22]. As illustrated in Figure 2.3b, when a magnetic field is applied along the easy axis the potential wells representing the spin-up and spin-down states shift in energy. As the magnetic field is swept, pairs of energy states from both wells will come into resonance. This resonance creates a channel for relaxation of the magnetization of the SMM. Therefore, the steps in the hysteresis curve correspond to an increase in the speed of magnetization relaxation as a result of tunnelling through these resonant channels [22]. As the temperature of the sample is increased, the spin state is thermally excited to higher energy levels, and subsequently require less of an increase in magnetic field to facilitate the tunnelling process. Quantum tunnelling of magnetization in a SMM is an example of a quantum phenomenon that can be seen even in measurements involving macroscopic samples.

2.3 Antiferromagnetic wheels

The Ferric wheel (Figure 2.4) is the prototypical AFW [67]. The chemical formula of this system is $[Fe(OCH_3)_2(O_2CCH_2Cl)]_{10}$. It consists of ten iron (III) ions arranged in a ring, with each metal centre participating in antiferromagnetic exchange interactions with each neighbouring metal ion. In general AFWs initially attracted interest due to their ability to serve as a model for one-dimensional magnetic materials. However, it was later proposed, and subsequently shown, that some of these systems will show quantum coherent oscillations of the Néel vector, once again displaying quantum phenomena on a larger scale [51, 79, 80]. In the ground state of an AFW the antiferromagnetic coupling between neighbouring ions results in each adjacent spin being oriented in an antiparallel configuration with the total spin $S = 0$. If one imagines the ring as being cut and unravelled into a linear chain of metal ions then the spin centres can be subdivided into two sublattices, with every second centre belonging to the same sublattice. The Néel vector then represents the overall spin state of the system as a function of the orientation of the magnetization vectors of each sublattice and is defined as:

$$\boldsymbol{n} = (\boldsymbol{M_A} - \boldsymbol{M_B})/(2M_0) \tag{2.2}$$

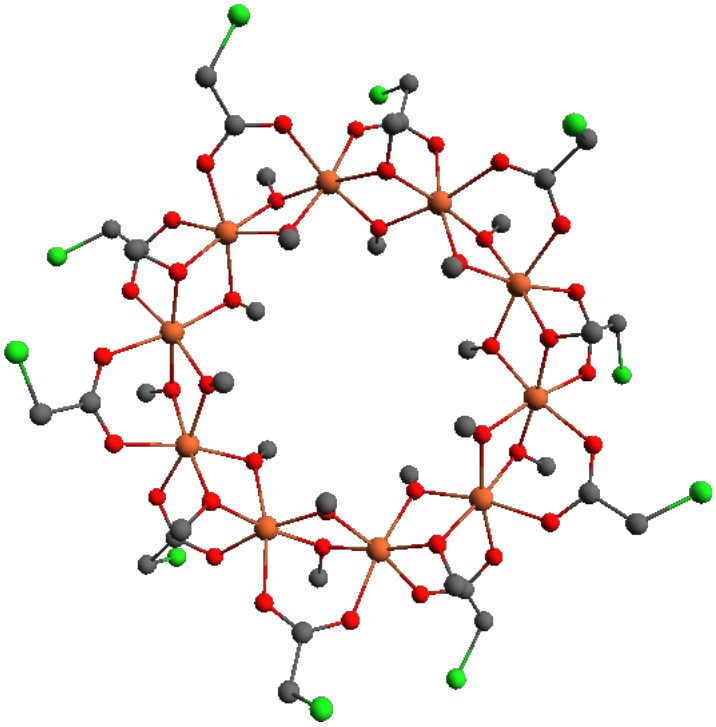

Figure 2.4: The chemical structure of the ferric wheel $[Fe(OCH_3)_2(O_2CCH_2Cl)]_{10}$ [67]. Neighbouring metal centres are antiferromagnetically coupled. Atom colours: Fe, orange; O, red; Cl, green; C, grey; hydrogen atoms are omitted for clarity.

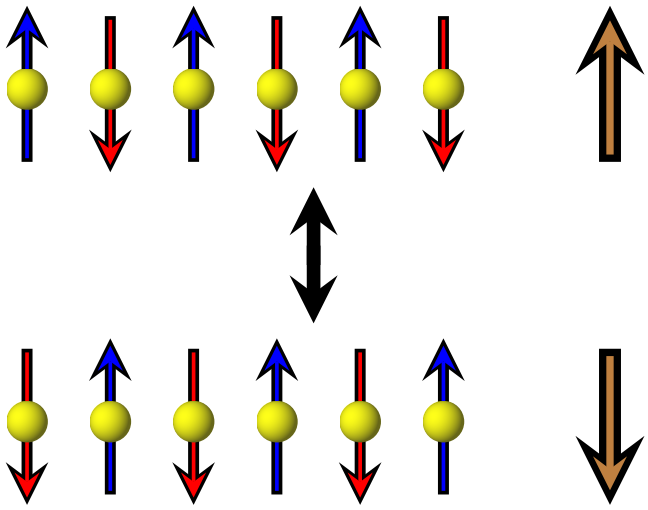

Figure 2.5: Quantum tunnelling of the Néel vector.

where $\boldsymbol{M_A}$ and $\boldsymbol{M_B}$ are the magnetization vectors of the two sublattices and M_0 is the length of the sublattice vectors. This Néel vector can be used to follow the spin dynamics of the system [51, 79, 80]. The tunnelling of the Néel vector between the two possible configurations of the AFW ground state is depicted in Figure 2.5.

We were initially drawn to the study of AFWs due to proposals that suggest that certain AFW systems could be used as potential qubits in an implementation of a quantum computer [74, 75]. The Cr_7Ni AFW specifically has a well separated, ground-state doublet that would represent a viable option for encoding as a qubit. Furthermore, through a series of pulsed ESR experiments, it has been shown that the coherence time of this nanomagnet is sufficiently long enough to allow for quantum operations to be performed reaching 3.8 μs for a perdeuterated analogue at 1.8 K [3]. However, we are primarily interested in utilizing the Cr_7Ni AFW as the molecular component in spintronics devices. Specifically, in addition to the coherence time being long enough to coherently manipulate the spin of the Cr_7Ni wheel, the spin relaxation time of the molecule is also sufficiently long enough to allow for the spin state of the system to be probed using a carbon nanotube mechanical resonator device [85] (see Section 5.1.2).

Chapter 3

The synthesis and characterization of an antiferromagnetic wheel

Chapter 3 of this thesis discusses the synthesis of an heterometallic antiferromagnetic wheel that is functionalized for the purpose of integrating the molecule into carbon-based nanoelectronics. The wheel is based on the Cr_7Ni molecular system. After introducing the chemical structure and reactivity of the general family from which the Cr_7Ni system is derived, I will comment in greater detail on our motivation for the synthesis, the outcome of the synthetic procedure, and how the synthesized molecule was characterized.

3.1 Introduction

As discussed in Chapter 2 of this thesis, there is significant interest in antiferromagnetic wheels (AFWs) due to the interesting quantum properties they exhibit. In particular, certain heterometallic AFWs, where an imbalance in spin has been created in the wheel by substituting one metal ion of a certain valency with a metal ion with a different spin, have shown that they possess a coherence time long enough to be used in quantum information processing [3]. The general structure of an AFW consists a number of metal ions arranged in a ring where each neighbouring metal centre is antiferromagnetically coupled. Surrounding this magnetic cluster are organic ligands that serve to isolate the magnetic core of the molecule and to mediate the coupling of the nanomagnet to its environment.

The organic shell surrounding the magnetic core plays an important role in determining the structure of the molecular nanomagnet and how the properties of the molecule can be utilized in the realization of spintronic devices. Functional groups can be introduced into the organic ligands in order to tailor the synthesized molecule for different applications. In some cases it is desirable to assemble subsystems of molecules that have various degrees of internal coupling. For example, a requirement of quantum information processing is the ability to generate entanglement between

multiple quantum systems. Furthermore, for the purposes of fabricating certain geometries of devices it may be necessary to create a thin film of nanomagnets, grafting the molecules to a surface. In order to link individual instances of a nanomagnet together, or to adhere the molecule to a certain substrate, specific functional groups must be incorporated into the organic ligands of the molecule.

We were interested in synthesizing a variant of the Cr_7Ni heterometallic AFW wheel with the ultimate goal of integrating the nanomagnet into a range of carbon-based nanoelectronic devices (see Chapter 5 of this thesis). Therefore, an understanding of the chemistry of the family of Cr_7Ni wheels was necessary in order to both decide which variant of the Cr_7Ni system to synthesize, and to know what additional functionalization of the molecule is possible in the future.

3.1.1 Chemical structure and reactivity

Motivated by theoretical work indicating that antiferromagnetic rings could exhibit coherent macroscopic quantum tunneling of magnetization [51], Larsen et al. (2003) synthesized a family of heterometallic rings that were based on the homometallic wheel $Cr_8F_8(O_2CC(CH_3)_3)_{16}$ (Cr_8-piv) [37]. The structure of Cr_8-piv consists of an eight membered ring of Cr^{3+} ions, where adjacent Cr centres are joined via two deprotonated pivalic acid ligands and a bridging fluoride. By replacing one of the Cr^{3+} ions with a dication metal a heterometallic anionic wheel is produced, which can be isolated in the presence of a cation. The chemical formula of the resulting system is:

$$[H_2R_2N][Cr_7MF_8(O_2CC(CH_3)_3)_{16}] \tag{3.1}$$

where the cation in the product is a secondary ammonium ion ($[H_2R_2N]$), and M refers to the metal dication substituted for a Cr centre. The impetus behind the formation of this product as opposed to the neutral homometallic ring is the coulombic attraction between the anionic wheel and the amine [72]. The secondary amine participates in hydrogen bonding with the bridging fluoride ligands, and serves as a template around which the ring is formed (Figure 3.1). Therefore, this synthetic strategy is an example of the templating method for synthesizing molecular nanomagnets [28]. The site of the substituted ion M^{2+} is disordered among the eight possible metal centres in the ring.

Several different species of this heterometallic wheel can be synthesized by varying any combination of the dication, the carboxylic acid or the secondary amine in the reaction. The unbalanced general chemical equation that represents this synthesis is given below:

$$CrF_3 \cdot 4\,H_2O + MX_2 + HNR_2 + \text{xs } HO_2CCR' \longrightarrow [H_2R_2N][Cr_7MF_8(O_2CCR')_{16}] + \ldots \tag{3.2}$$

The wheel is made by combining chromium (III) fluoride tetrahydrate with a dication metal salt, a secondary amine and an excess (xs) of a carboxylic acid (pivalic acid

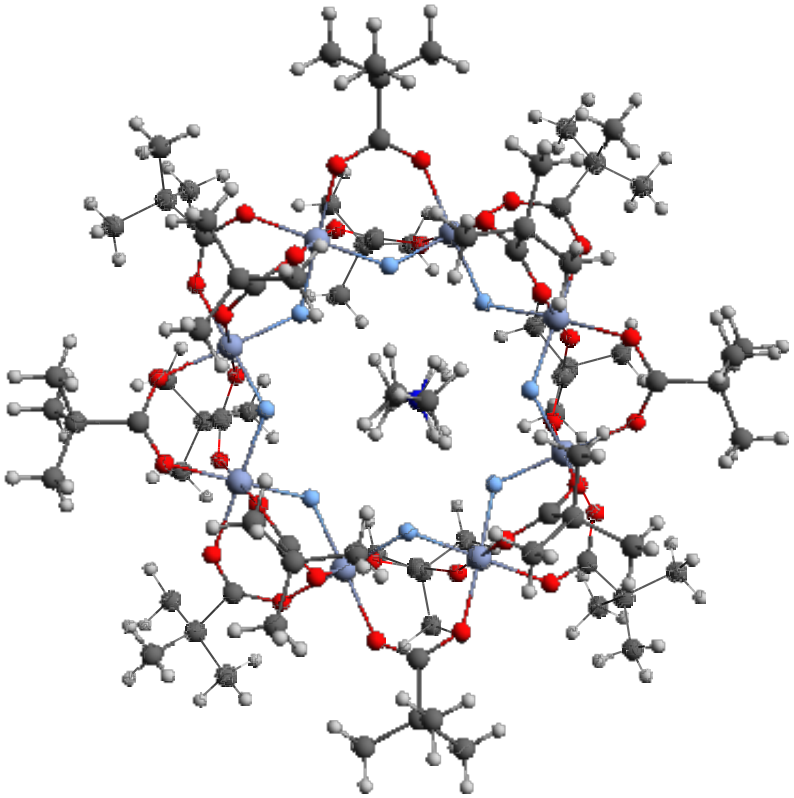

Figure 3.1: The structure of $[H_2R_2N][Cr_7MF_8(O_2CC(CH_3)_3)_{16}]$. The amine sits in the centre of the ring and participates in hydrogen bonding with the bridging fluorines [37]. Atom colours: Cr/Ni, purple; F, blue; O, red; C, grey; H, white.

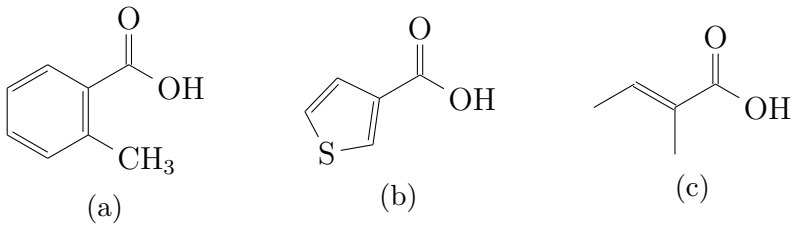

Figure 3.2: A sample of some of the carboxylic acids that have been successfully used in the synthesis of derivatives of Cr_7Ni in the literature (a) 2-methylbenzoate, (b) 3-thiophenecarboxylate, (c) trans-2,3-dimethylacrylate.

was used in the description of the structure in the preceding paragraph). This reaction will produce a family of products, including the neutral homometallic Cr_8-piv wheel, from which the desired molecule can be isolated [37]. By varying the identity of the dication the magnetic properties of the nanomagnet as well as its ring structure can be altered [37, 38]. We were interested in working with the Ni derivative of this molecular nanomagnet (Cr_7Ni), and thus in general it should be assumed that MX_2 in the above reaction represents the Ni salt $2\,NiCO_3 \cdot 3\,Ni(OH)_2 \cdot 4\,H_2O$ (nickel carbonate hydroxide tetrahydrate).

There exist many chemical strategies for integrating functional groups into the organic shell of the Cr_7Ni nanomagnet, some of which are described in the following sections.

The carboxylate ligand

There are two possible methods for varying the carboxylate ligands in the Cr_7Ni molecule: either a different carboxylic acid can be used at the outset of the synthesis, or a carboxylate displacement reaction can be carried out after the nanomagnet has already been made. The first method will result in a ring where all of the carboxylate ligands are the same, while in the second technique one of the ligands will be substituted. A wide variety of carboxylic acids have been successfully used in the initial synthesis of the Cr_7Ni ring [41]. The structures of some of these reagents are given in Figure 3.2.

Due to the relative reactivities of Cr^{3+} and Ni^{2+} a carboxylate displacement reaction will result in the *selective* replacement of one of the carboxylate ligands in the ring. The Cr^{3+} valency is one of the least reactive 3d-metal ions due to its d^3 configuration. Therefore, if a carboxylate displacement reaction is carried out on Cr_7Ni one of the four bridging carboxylate ligands attached to the Ni site will be the ligand that is displaced [72]. Considering the carboxylate group is also bonded to a Cr^{3+} ion the reaction has to be forced. By dissolving the molecular nanomagnet along with the desired carboxylic acid in an organic solvent and refluxing, an existing carboxylate ligand can be replaced with one containing a useful functional group [71]. The resulting species can then be separated from the original ring using

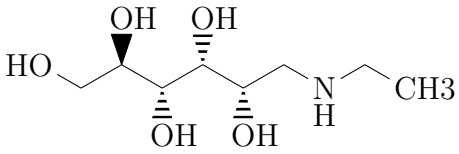

Figure 3.3: The chemical structure of *N*-ethyl-D-glucamine.

chromatographic techniques.

The amine

The secondary amine acts as a template in the synthesis of the Cr_7Ni nanomagnet, sitting in the centre of the ring and participating in hydrogen bonding with the fluoride ligands. By varying the alkyl chains of the amine used in the synthesis a wide range of functional groups can be introduced. For example, when $[CH_3CH_2NH_2CH_2py]$ is added to the reaction the ring forms around the amine, allowing the pyridine nitrogen to bond to other molecular species [1].

Furthermore, by incorporating amines with branched chains, derivatives of Cr_7Ni are obtained consisting of nine and ten membered rings [70]. An even more dramatic result occurs when the polyol *N*-ethyl-D-glucamine ($C_8H_{14}NO_5H_5$) (Figure 3.3) is used as the secondary amine in the reaction. In this case the polyol becomes deprotonated and replaces several of the fluoride ligands in the ring, producing a terminal ligand that can be used to link the AFW to other groups [73].

Linking multiple Cr_7Ni nanomagnets together

As mentioned above, the ability to couple individual nanomagnets together is a requirement of certain proposals for the use of these molecular systems in quantum information processing. To that end, utilizing some of the techniques discussed in the preceding sections on functionalizing Cr_7Ni, several results have been presented where multiple nanomagnets have been linked, either directly [1] or through an intermediate metal cluster [73, 71]. Though the dimer produced by simply using a diamine in the reaction exhibited no coupling between the individual nanomagnets [1], by connecting the molecules via a metal cluster attached to functionalized carboxylate ligands, Timco et al. (2009) were able to demonstrate a link between the two molecules via electron spin resonance (ESR), specific heat, and magnetic susceptibility measurements [71]. Furthermore, the authors were able to show how by varying the metallic cluster between the nanomagnets the coupling of the molecules could be altered [71].

By combining multiple techniques, elegant and elaborate structures containing different subsystems of molecular nanomagnets have been synthesized [4, 82, 83]. All of these results indicate the wealth of possibilities for functionalizing and constructing complex subsystems of these molecules. Furthermore, the interplay between

the structures of these complexes and their physical properties illustrates the interdisciplinary nature of this research; the tools of chemistry can be used to produce systems on which interesting physics can be explored.

3.2 Synthesis and characterization of Cr_7Ni-eth

The device proposal that initially motivated our research utilizes a carbon nanotube (CNT) resonator to probe the spin state of a molecular nanomagnet [85]. In order to meaningfully probe the spin state of a nanomagnet coupled to the mechanical oscillations of a CNT, the coherence time of the molecular system must be sufficiently longer than the time required to perform a measurement on the device. For the device described by Willick et al. (2014) the measurement time scale is no longer than $\sim$300 μs [85], and can be made smaller by tuning the parameters of the CNT. Therefore, the approximately 1 ms spin relaxation time of the Cr_7Ni AFW allows its spin state to be investigated by the proposed hybrid device [3].

Consequently, we were interested in synthesizing a variant of the Cr_7Ni heterometallic AFW that would be capable of being grafted to a CNT. As described in the preceding section, the chemistry of the Cr_7Ni wheel is very rich, with numerous possibilities for both incorporating functional groups into the molecule and for assembling more complex subsystems and supramolecular structures. The molecular system synthesized would need to be grafted to the nanotube. Rather than covalently bonding to the CNT, which could negatively disrupt the properties of both the nanomagnet and the nanoelectronic components, weaker forces such as van der Waals forces and π-π stacking interactions could be exploited. To that end, the molecule synthesized was required to be functionalized with either long alkyl chains or pyrene containing ligands.

Ghirri et al. (2010), demonstrated that a derivative of the Cr_7Ni nanomagnet synthesized by substituting 2-ethylhexanoic acid in the place of pivalic acid was capable of grafting to bulk graphite through non-covalent interactions [30]. Following this recipe, we used 2-ethylhexanoic acid (pictured in Figure 3.4) instead of pivalic acid in the synthesis of the compound, producing the structure illustrated in Figure 3.4 with the chemical formula $[H_2R_2N][Cr_7NiF_8(C_8H_{16}O_2)_{16}]$ ($Cr_7Ni{-}eth$). We anticipated that the long alkyl chains of 2-ethylhexanoic acid will interact with the CNT via van der Waals forces, forming non-covalent bonds, and leaving the mechanical and electronic properties of the CNT, as well as the magnetic properties of the nanomagnet, intact [24].

Synthesis

Two variations of Cr_7Ni-eth were synthesized: in the first procedure diethylamine was used as the secondary amine in the reaction, while in the second synthesis, dipropylamine was added instead. For the remainder of this thesis, $Cr_7Ni{-}eth$

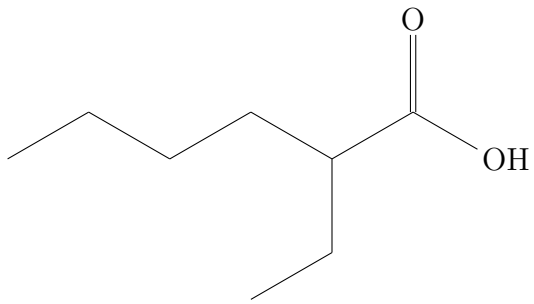

(a)

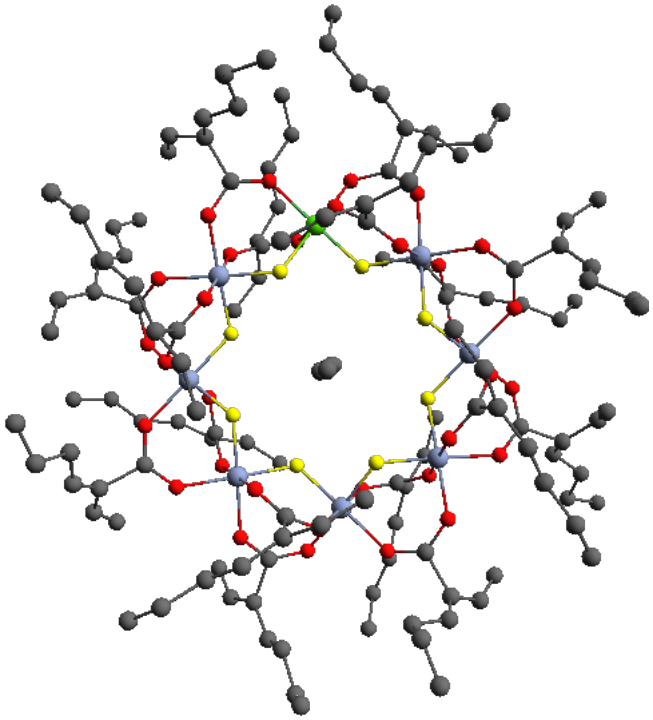

(b)

Figure 3.4: The chemical structure of (a) 2-ethylhexanoic acid and (b) Cr_7Ni−eth; in the above structure di-n-propylamine was the amine used in the reaction [30]. Atom colours: Cr/Ni green; F yellow; O red; C black; N cyan.

(p) will be used to refer specifically to the dipropylamine product while Cr_7Ni-eth will refer to the product synthesized using diethylamine. The synthetic procedure followed the process outlined in Ghirri et al. (2010). All reagents and solvents were purchased from commercial sources and were not additionally purified in any way. The reactions were carried out in a Teflon round-bottomed flask.

For both of the syntheses, the desired product was isolated using column chromatography. A series of thin layer chromatography (TLC) experiments were performed to determine an optimum solvent mixture to run the column. Based on the results of the TLC plates an eluent mixture of 2:1 chloroform:hexane was selected for the diethylamine product, and a mixture of 1:1 dichloromethane:hexane was used for the dipropylamine product. The desired compound was the second band collected. A second column was run on certain fractions of the band collected for the diethylamine product to isolated more of the desired compound using a 5:1 chloroform:hexane solvent mixture.

Two methods were used in an attempt to grow a single crystal of the synthesized product. In the first technique, a small amount of the separated material was placed in a vial with a solvent, and the vial was then sealed with a lid containing a rubber septum. The septum was punctured allowing the solvent to slowly evaporate. Several solvents were tested with acetone being the only solvent that resulted in the growth of a crystal. However, all of the crystals grown using acetone were twinned.

In the second technique, a small amount of the material was placed in a vial and dissolved in a solvent. That vial was then placed in a larger vial containing a second solvent within which the product was less soluble. The idea behind this method is that as the two solvents diffuse and mix, the material will come out of solution forming a crystal. Unfortunately, this technique never yielded a positive result.

Characterization

The synthesis product was characterized using x-ray diffraction (XRD), electron spin resonance (ESR) spectroscopy, Fourier transform infrared spectroscopy (FTIR), and Raman spectroscopy. All FTIR spectra were obtained using a Bruker Tensor 27 spectrometer. The sample was prepared for FTIR analysis as a KBr pellet using KBr powder bought from Sigma Aldrich that was dried in the oven prior to use. The Raman spectra were measured using a Horiba Jobin Yvon HR800 spectrometer equipped with three laser light sources at 532.06 nm, 632.817 nm, and 785.83 nm, and an Olympus BX41 microscope. The ESR spectra were acquired using a Bruker EMXmicro spectrometer.

The characterization of the synthesized product served two main goals: to confirm that the synthesized molecule was the desired Cr_7Ni-eth system, and to obtain data to fingerprint the molecule for future experiments. As previously mentioned, the ultimate goal of this research is to integrate the Cr_7Ni-eth molecule into spintronics devices to be studied using quantum transport techniques. The behaviour of these devices will largely depend on both the structural and magnetic properties

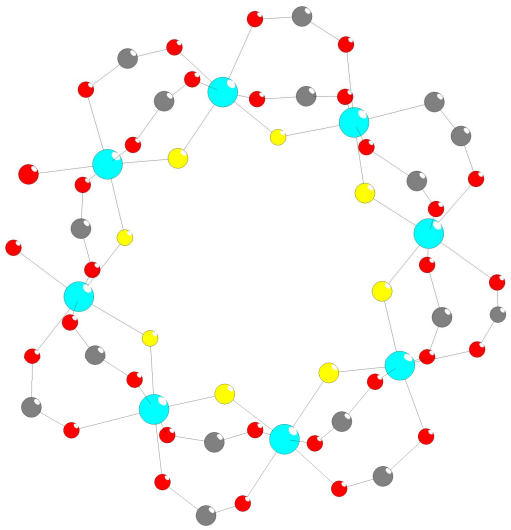

Figure 3.5: The partial structure obtained from XRD. Atom colours: Metal centres, turquoise; F, yellow; O, red; C, grey.

of the Cr_7Ni-eth wheel, and thus it is important to obtain data that demonstrates the properties of this molecule in order to be able to interpret the results of future quantum transport experiments. Furthermore, fingerprint data of the Cr_7Ni-eth system can also be utilized to answer the question of whether the system retains its structural and magnetic properties when integrated into nanoelectronic devices (e.g. are Raman peaks characteristic of the molecule present in the Raman spectrum of the molecule deposited on a graphene substrate).

X-ray diffraction

X-ray diffraction was run on a crystalline sample of the synthesis product grown from the slow evaporation of an acetone solution. Unfortunately, we were unable to grow a crystal that was not twinned and as a result the structures obtained from all XRD experiments were incomplete. Figure 3.5 illustrates the partial structure obtained from the a crystal. Although the complete structure was not measured, we were able to confirm the presence of the metal ring found in the AFW. The parameters of the unit cell were measured and are given in Table 3.1.

Raman and FTIR

We measured both the Raman and the FTIR spectrum of the synthesized Cr_7Ni-eth product. In addition to collecting evidence to confirm that Cr_7Ni-eth was indeed

	Measured	Expected
Space Group	$P\bar{1}$	$P\bar{1}$
a (Å)	20.47	19.5623(13)
b (Å)	25.20	25.0121(17)
c (Å)	33.45	34.506(2)
α	84.27	68.9470
β	89.65	89.5650
γ	74.14	87.7690

Table 3.1: The measured and expected parameters of the $Cr_7Ni-eth$ unit cell. The expected parameters were taken from [30]

isolated and the synthesis was succesful, it was important to obtain fingerprint data for the molecule. One of the open questions of this research is whether the molecular system will retain its structural stability when grafted to a carbon nanostructure. By comparing the vibrational spectrum of the free molecule to that of the molecule when grafted to a graphene surface we can determine whether the system retains its structural stability.

It has been reported that certain single-molecule magnets are vulnerable to laser damage, which causes a broadening of the peaks in the measured Raman spectrum [55, 47]. Additionally, the Cr_7Ni-eth molecular nanomagnet does not possess a strong Raman signal. Consequently, in order to successfully record the spectrum, longer acquisitions times (240 s) and low laser power were required.

The Raman spectrum of Cr_7Ni-eth is shown in Figure 3.6 and the FTIR spectrum of Cr_7Ni-eth is given in Figure 3.7. The FTIR spectrum of Cr_7Ni-eth (p) and a previously synthesized AFW Cr_7Mn-piv is included in Appendix A.

Electron spin resonance

The ESR spectrum of a crystalline sample of $Cr_7Ni-eth$ measured at 4K is given in Figure 3.8. This spectrum will be discussed in more detail in Chapter 4 of this thesis, but the resonances present are consistent with what is expected for Cr_7Ni-eth. There are two prominent resonances in the spectrum at $g = 1.770$ and $g = 1.975$.

3.3 Fluorescent single-molecule magnets

In addition to synthesizing the AFW Cr_7Ni-eth, through collaborations with another research group we were able to obtain a few variations of a SMM family that are unique in that they contain fluorescent ligands that retain their fluorescent properties when attached to the magnetic, metal cluster [65, 2]. The general chemical formula for this SMM is $[Mn_3O(O_2CCH_3)_3(mpko)_3](ClO_4)^-$, where mpkoH is methyl 2-pyridyl ketone oxime. These SMMs consist of three ferromagnetically

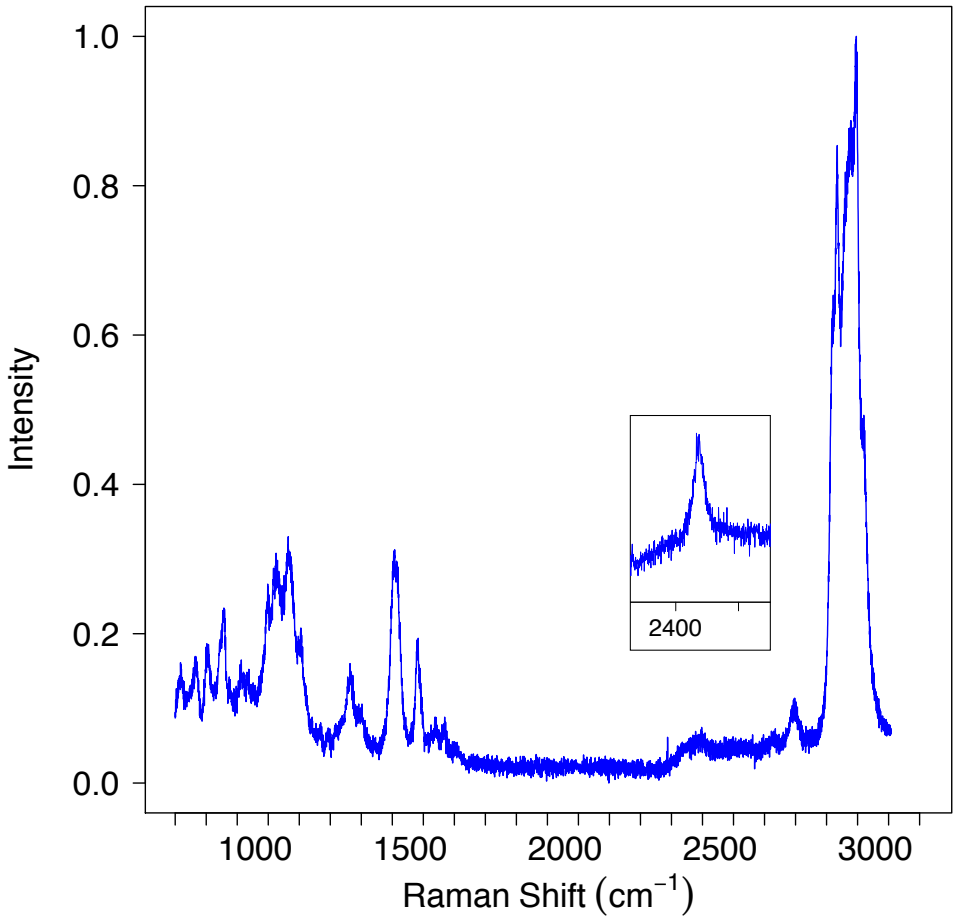

Figure 3.6: The Raman spectrum of a powder sample of Cr_7Ni-eth. The spectrum pictured was obtained using a laser power of ($\sim$ 1.5 mW) with an acquisition time of four minutes. This power level might be too large, and potentially damaging to the molecular nanomagnet, as the peak at 2400 cm^{-1} has broadened considerably compared to the same peak at a lower power ($\sim$ 60 μW; see inset).

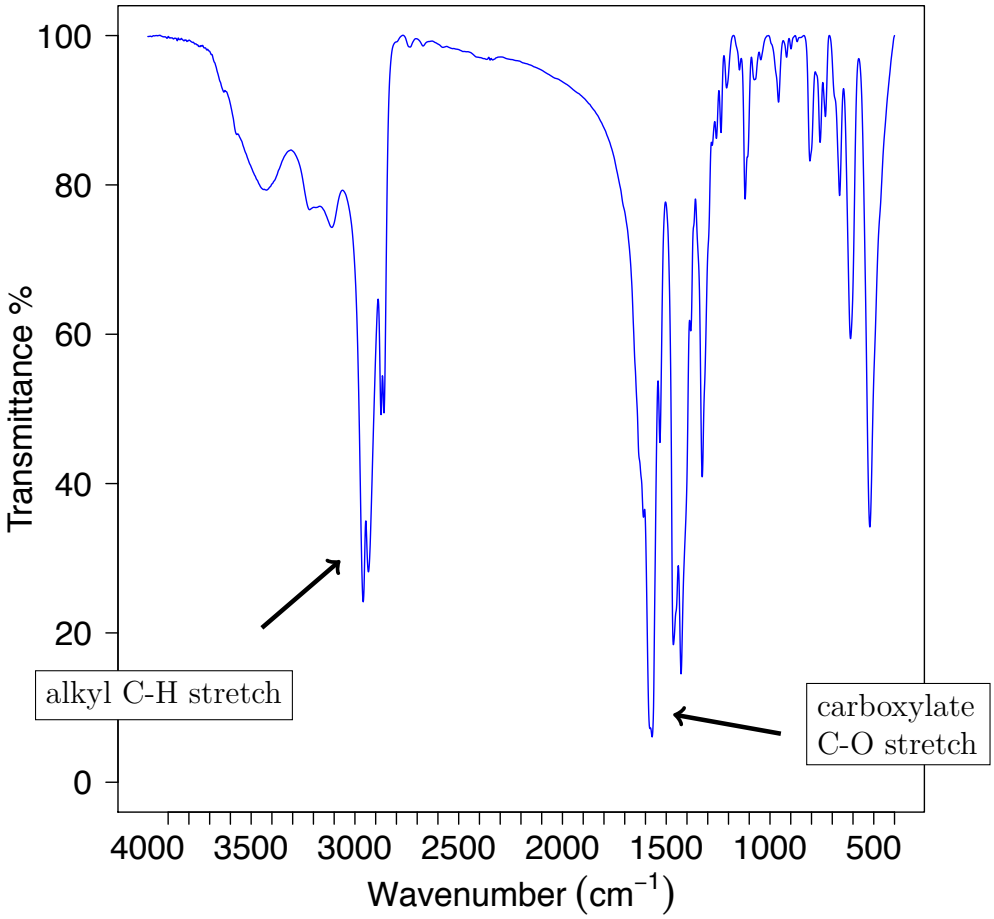

Figure 3.7: The FTIR spectrum of a KBr pellet of Cr_7Ni-eth. The cluster of peaks around 2900 cm^{-1} are characteristic of C-H stretching in 2-ethylhexanoic acid. As well the peak at approximately 1570 cm^{-1} indicates the presence of a carboxylate ion in the molecule.

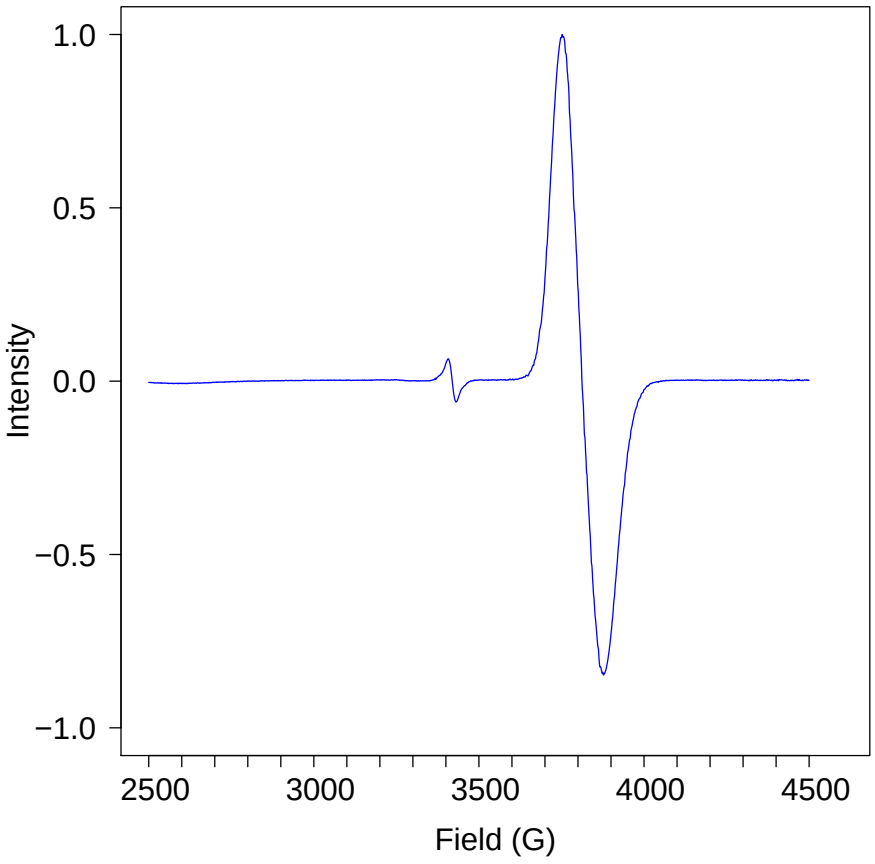

Figure 3.8: The ESR spectrum of a crystalline sample of Cr_7Ni-eth at 4K. There are two resonances in the spectrum corresponding to $g = 1.770$ and $g = 1.975$.

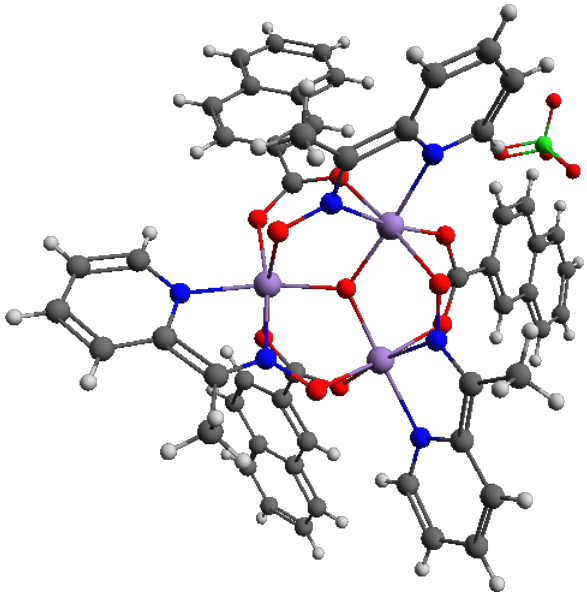

Figure 3.9: The structure of the Mn_3−naph SMM [2]. Atom colours: Mn, purple, O, red; N, blue; C, grey; Cl, green; H, white.

coupled Mn^{3+} ions arranged in a triangular geometry. Typically triangular metallic clusters do not behave as SMMs as the metal ions tend to be antiferromagnetic coupled, resulting in a small S ground state. However, for the Mn_3 family of molecules a ligand-imposed structural distortion forces a ferromagnetic exchange interaction between the metal centres causing a high-spin, $S = 6$ ground state [65]. The Mn_3 SMMs we have obtained have been functionalized with fluorescent ligands containing pyrene, anthracene and naphthalene groups. The structure of the naphthalene derivative is given in Figure 3.9.

3.3.1 Characterization

The Mn_3 SMMs were characterized using FTIR and Raman spectroscopy. Similar to Cr_7Ni-eth the vibrational spectra of these molecules were obtained in order collect fingerprint data to determine the structural stability of the nanomagnets after they have been grafted to a carbon nanostructure. Furthermore, considering the SMM properties of the Mn_3 family are dependent on ligand-induced structural distortions, whether or not these systems retain their magnetic properties when grafted to a surface is also an interesting research question. Similar to the Cr_7Ni-eth molecular nanomagnet, the Mn_3 family did not possess a strong Raman signal and were potentially vulnerable to the power of the laser. Consequently, in order to measure the spectra long acquisitions times and low power were required. The Raman spectrum of Mn_3-naph and the FTIR spectrum of all of the members of the Mn_3 family

are included in Appendix A.

3.4 Discussion

We have synthesized two derivatives of the Cr_7Ni-eth AFW that contain ligands with long alkyl chains for the purpose of integrating the molecules into molecular spintronics devices. The products of the synthesis were characterized using a combination of XRD, FTIR and Raman spectroscopy, and ESR spectroscopy. Although the results of the XRD experiments did not give a complete structure we were able to verify the presence of the eight-membered metallic ring. Furthermore, the measured space group is the same as what was expected, as taken from [30]. Although the remaining unit cell parameters were not in complete agreement (see Table 3.1) this discrepancy could potentially be explained by the fact that the product we were able to crystallize contained a different templating amine: diethylamine as opposed to dipropylamine. In addition to the XRD data that verified the presence of the metal wheel, the measured ESR data is in agreement with what is expected for the Cr_7Ni family of molecules (see Chapter 4 of this thesis). Consequently, based on these results we believe that the magnetic core is the heterometallic Cr_7Ni ring.

The FTIR spectrum was collected for both of the synthesized derivatives. The primary purpose for studying the vibrational spectra of the molecules was to obtain fingerprints of the systems, in order to determine whether the molecules remain structurally intact when deposited on graphene surfaces. The FTIR spectrum of the diethylamine derivative also provided further evidence that the synthesized product was in fact the desired Cr_7Ni-eth compound. Although the majority of the spectrum is difficult to assign, the pattern of the peaks around 2900 cm^{-1} that correspond to alkyl C-H stretching in the molecule, closely resembles that of 2-ethylhexanoic acid, the carboxylic acid involved in this synthesis. Furthermore, the absence of a carboxylic peak around 1700 cm^{-1}, and the appearance of a carboxylate stretching peak around 1570 cm^{-1} confirms the presence of the deprotonated carboxylate ligand in the molecule. The Raman spectrum of Cr_7Ni-eth also contains peaks around 2900 cm^{-1} that can also be assigned to alkyl C-H stretching.

As previously mentioned, the ultimate purpose of synthesizing the Cr_7Ni-eth AFW is to integrate this molecular system into carbon-based spintronics devices, such as a CNT nanoelectromechanical resonator (see 5.1.2). Depending on the results of our first attempts to graft the AFW to carbon nanostructures, the Cr_7Ni-eth derivative of the Cr_7Ni can be further functionalized as required. For example, if the grafting is unsuccessful longer alkyl chains may need to be integrated into the organic shell of the system. A carboxylate displacement reaction could also potentially be carried out to replace one of the 2-ethylhexanoic acid ligands with a ligand containing π-π stacking groups (e.g. 1-pyrenecarboxylic acid), which would also increase the ability of the molecule to be grafted to carbon nanostructures. It is important to consider that the transport properties of any device incorporating the

Cr_7Ni-eth AFW will depend in part on the nature of the organic ligands present in the molecule [9]. For example, in a molecular transistor with a break-gap junction geometry the presence of longer alkyl chains attached to the magnetic core of the system will increase the tunnel barriers between the electrodes and the molecule in the junction. Through common organic synthesis techniques one has a great deal of control over customizing the structure of these AFW species, and thus an instance of these wheels can be explicitly tailored for a specific application.

Chapter 4

The electron spin resonance spectra of molecular nanomagnets

Chapter 4 of this thesis discusses experiments conducted to study the magnetic properties of the Cr_7Ni-eth antiferromagnetic wheel synthesized in Chapter 3, as well as the properties of the Mn_3 family of single-molecule magnets obtained through collaborations with other research groups. The magnetic spectrum of the nanomagnets were probed using continuous wave electron spin resonance (CW-ESR), and were simulated using an appropriate spin Hamiltonian.

4.1 Introduction

Describing the correlation between the electronic structure of a molecular system and the magnetic interactions present in the molecule from first principles, such as by using density functional theory or other *ab initio* methods, is non-trivial, and for many systems unnecessary. A spin Hamiltonian approach can be utilized to understand many of the salient features present in the magnetic energy spectrum of a molecule [28]. The parameters of the Hamiltonian are extracted by fitting experimental data, and can then be applied to interpret the results of further magnetic studies of the system of interest. Furthermore, knowledge of the magnetic energy spectrum of a given molecular nanomagnet would also be useful for interpreting results of quantum transport experiments on spintronics devices that contain the same nanomagnet.

In constructing the spin Hamiltonian the spatial components of the wavefunction are assumed to be adequately taken into account by constant magnetic parameters, leaving only the spin coordinates of the system to be described by electron spin and nuclear spin vector operators. This approach makes several approximations, the principal one being that orbital angular momentum can effectively be treated as a perturbation to the system. For a system with an orbitally non-degenerate ground state this approximation is typically valid, and the spin Hamiltonian approach is an

effective tool for constructing the magnetic energy spectrum of the system [28].

Diagonalizing the full spin Hamiltonian of a large spin cluster such as a molecular nanomagnet to obtain the energy levels of each magnetic state in the system can be computationally unrealistic. For example, the dimensions of the spin Hamiltonian of the $Mn_{12}-$actetate single-molecule magnet (SMM) is $\approx 10^8 \times 10^8$. Two different approaches have been utilized in the literature to address this problem: either a mathematical technique has been applied to simplify the diagonalisation procedure (e.g. utilizing the formalism of irreduscible tensor operators [13], or an effective Hamiltonian has been constructed that reduces the dimension of the problem [7]. In the following section I will describe two different forms of the spin Hamiltonian: the coupling single-ion Hamiltonian, and the effective Hamiltonian produced using the giant spin approximation.

4.1.1 The spin Hamiltonian

Giant spin approximation

In the giant spin approximation (GSA) the ground state energy level is assumed to be well isolated from the excited states of the molecule. Following this approximation the total spin S is assumed to be a good quantum number, with no S-mixing occurring between the ground states and the excited states. An effective Hamiltonian can then be defined to model the lowest $(2S+1)$ states of the system. This spin Hamiltonian takes the general form

$$\hat{\mathcal{H}}_{GSA} = \sum_{k=0,2,4,\ldots} \sum_{m=0}^{k} B_k^m \hat{O}_k^m(\hat{S}_z, \hat{S}_\pm) + \mu_B \vec{B} \cdot \overleftrightarrow{g} \cdot \hat{S} \tag{4.1}$$

where B_k^m are the parameters associated with the Stevens operators $\hat{O}_k^m(\hat{S}_z, \hat{S}_\pm)$. Utilizing the Stevens operators is an effective method for incorporating higher order terms of the traditional spin operators S_z, S_x and S_y that takes advantage of point group symmetry present in the molecular system. The second term of the above Hamiltonian corresponds to the Zeeman energy, where μ_b is the Bohr magneton, $\vec{B}$ is the applied magnetic field, $\overleftrightarrow{g}$ is the g-tensor and $\hat{S}$ is the spin vector operator $(\hat{S}_x,\hat{S}_y,\hat{S}_z)$.

The specific Stevens operators from the sum in (4.1) to be included in the spin Hamiltonian will depend on the symmetry of the molecule being investigated. For a molecule with spherical symmetry, there will be no anisotropic effects, and only the Zeeman interaction will be relevant. In systems with lower symmetry, higher order terms will need to be included in order to account for the anisotropic interactions. If the second order Stevens operators are included, the Hamiltonian can be simplified to the familiar form

$$\hat{\mathcal{H}}_{GSA} = D\hat{S}_z^2 + E(\hat{S}_x^2 - \hat{S}_y^2) + \mu_B \vec{B} \cdot \overleftrightarrow{g} \cdot \vec{\hat{S}} \tag{4.2}$$

where the parameters D and E can be expressed using the Stevens parameters B_k^m as $3B_2^0$ and B_2^2 respectively. This Hamiltonian would be applied to a system with rhombic symmetry.

The GSA is valid in the strong exchange limit where the ground state is well isolated from the excited states of the system. However, as the anisotropic effects in the system begin to approach the energy scale of the exchange interactions between the metal ions in the cluster, higher order terms are required in order to account for the S-mixing that will occur between the ground state and the excited states of the molecule. As more terms are added, the model can become over-parameterized, making it no longer useful when it comes to interpreting experimental magnetic data [86].

Coupling single-ion Hamiltonian

The coupling single-ion Hamiltonian models the magnetic interactions within a molecule based on the contributions to these interactions by each individual ion in the cluster. The general form of this Hamiltonian is given by

$$\hat{\mathcal{H}} = \hat{\mathcal{H}}_{ZE} + \hat{\mathcal{H}}_{exchange} + \hat{\mathcal{H}}_{anisotropic} \tag{4.3}$$

The first term in (4.3) is a sum of the Zeeman energies of each inidividual ion in the cluster, and $\hat{\mathcal{H}}_{anisotropic}$ is a sum of the single-ion anisotropic contributions. $\hat{\mathcal{H}}_{exchange}$ can be further broken down to

$$\hat{\mathcal{H}}_{exchange} = \hat{\mathcal{H}}_{isotropic} + \hat{\mathcal{H}}_{symmetric} + \hat{\mathcal{H}}_{antisymmetric} \tag{4.4}$$

where the latter two terms in (4.4) refer to anisotropic exchange interactions between the different ions in the cluster.

The dominant term in (4.4) is the isotropic exchange interaction, given by

$$\hat{\mathcal{H}}_{isotropic} = -2 \sum_{i,j>i} \hat{S}_i J_{ij} \hat{S}_j \tag{4.5}$$

In this formalism a positive value for the exchange constant J_{ij} indicates a ferromagnetic interaction between ions i and j, while a negative value for J_{ij} is representative of an antiferromagnetic exchange. The sum in (4.5) is over all of the different possible pairs of ions in the cluster. The most basic form of the coupling single-ion Hamiltonian only takes into account isotropic interactions giving

$$\hat{\mathcal{H}}_{iso} = -2 \sum_{i,j>i} \hat{S}_i J_{ij} \hat{S}_j + \sum_i g_{iso,i} \vec{B} \mu_B \vec{\hat{S}}_i \tag{4.6}$$

For a system with N equivalent spins, S, the dimensions of the coupling single-ion Hamiltonian will be equal to $(2S+1)^N$. Consequently, as previously stated, for large molecular systems, diagonalizing this Hamiltonian will become computationally infeasible. However, if this linear algebra problem can be solved, as it can be for the systems we are interested in studying, the single-ion Hamiltonian will allow one to gain information concerning how the individual ions in the metal cluster contribute to the overall magnetic properties of the molecule.

4.2 The magnetic spectrum of Cr_7Ni-eth

The magnetic spectrum of the Cr_7Ni-eth antiferromagnetic wheel was simulated using the coupling single-ion Hamiltonian. With seven Cr^{3+} ions ($S = 3/2$) and one Ni^{2+} ion ($S = 1$) the dimensions of the full Hamiltonian describing this system are on the order of $10^4 \times 10^4$. This size of matrix is within the limits of what is practically diagonalizable for modern computers. The simulations of the magnetic spectrum of the nanomagnet were coded in MATLAB, taking advantage of the ARPACK implementation of the eigenvalue problem to further improve the efficiency of the diagonalization. ARPACK is a collection of functions designed to solve large eigenvalue problems [42]. The package of software implements a variation of the Arnoldi/Lanczos algorithm to solve for a subset of the eigenvalues of a sparse, symmetric matrix.

As a first approximation for fitting the simulated magnetic energy spectrum to experimental CW-ESR data, only the isotropic terms were included in the single-ion Hamiltonian. Furthermore, it was assumed that only nearest neighbour exchange interactions were significant, and the z-axis was chosen to coincide with the applied magnetic field. With these assumptions the single-ion Hamiltonian becomes:

$$\hat{\mathcal{H}}_{iso} = -2 \sum_{i,j=i+1}^{N} \hat{S}_i J_{ij} \hat{S}_j + \sum_i g_{iso,i} B_z \mu_B \hat{S}_{z,i} \tag{4.7}$$

where in the exchange summation $N + 1 = 1$ (i.e. the ring is closed) and $g_{iso,i}$ is the isotropic g-factor of the i^{th} ion in the molecular nanomagnet.

The zero-field splitting of the first 44 energy levels of the Cr_7Ni-eth antiferromagnetic wheel is given in Figure 4.1 where the energy of the ground state is set at $E = 0$. As determined from inelastic neutron scattering experiments [10], values of $J_{Cr-Cr} = J_{Cr-Ni} = -5.77$ cm^{-1} were used as the exchange parameters in the Hamiltonian. The molecular structure of the Cr_7Ni-eth wheel is also pictured in Figure 4.1. Recall, this molecule consists of a ring of eight metallic centres, seven Cr^{3+} ions and a single Ni^{2+} ion, antiferromagnetically coupled through a superexchange interaction mediated by bridging oxygen atoms. Based on the electron configuration of the chromium and nickel ions, the Cr^{3+} ions are each $S = 3/2$ species, while the Ni^{2+} ion is $S = 1$.[1] Given the imbalance in electron spin, the magnetic ground state is expected to be a doublet with $S = 1/2$. This multiplicity is borne out in the diagonalization of the isotropic single-ion Hamiltonian. The molecule is characterized by a $S = 1/2$ ground state, with a lowest-lying excited state found 9.60 cm^{-1} (~ 1.18 meV) above the ground state.

The full magnetic energy spectrum up to 8000 G is given in Figure 4.2. Only the lowest-lying 16 eigenstates of the system are plotted. Isotropic g-values were used for the chromium ions and the nickel ion: $g_{Cr} = 1.96$ and $g_{Ni} = 2.25$ [59]. As

[1] Electron configuration of Cr^{3+}: [Ar]3 d^3, three unpaired electrons, $S = 3 \times 1/2 = 3/2$; electron configuration of Ni^{2+}: [Ar]3 d^8, two unpaired electrons, $S = 2 \times 1/2 = 1$

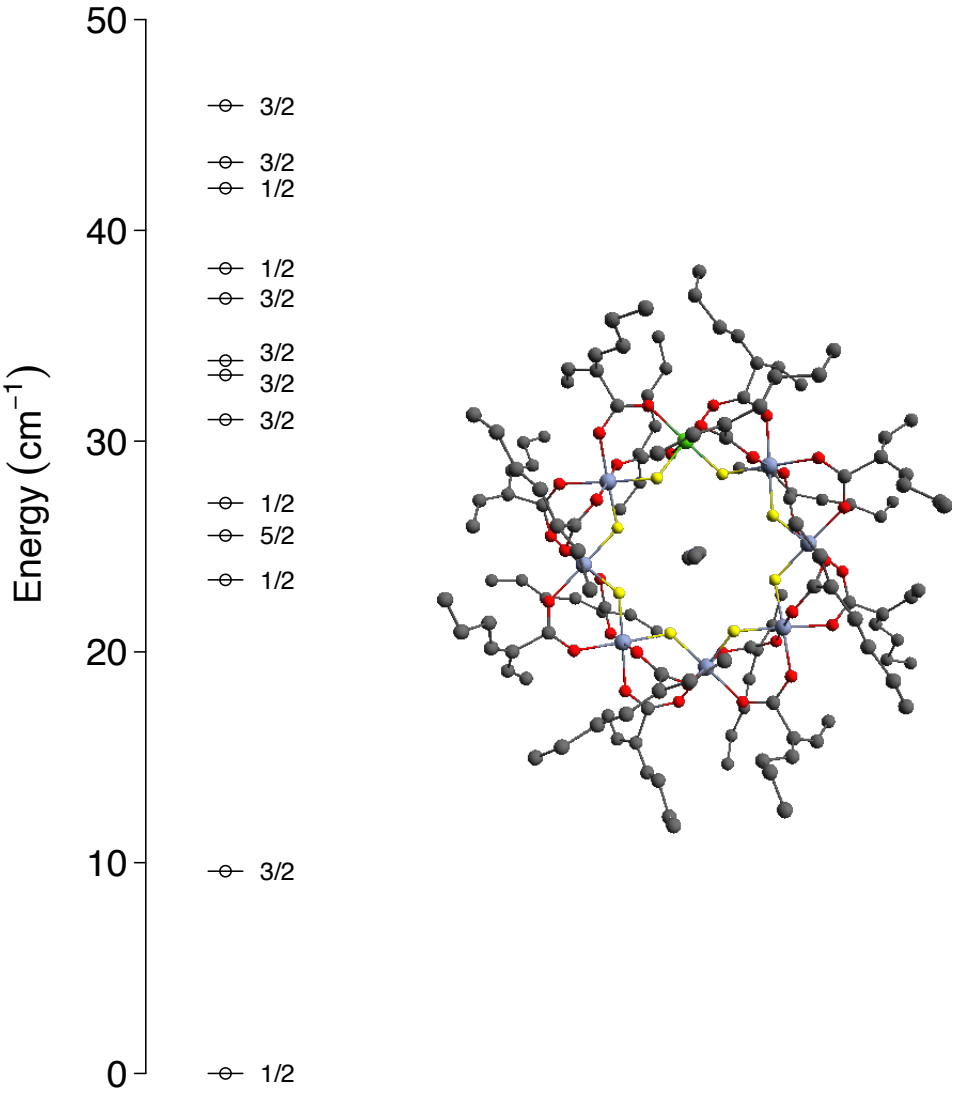

Figure 4.1: The zero-field energy spectrum of Cr_7Ni−eth simulated using the coupling single-ion Hamiltonian. The spectrum is characterized by a $S = 1/2$ ground state, and a $S = 3/2$ first excited state 9.60 cm^{-1} above the ground state. The Cr_7Ni−eth wheel is pictured to the right of the spectrum. Recall, this molecule consists of seven Cr^{3+} ions ($S = 3/2$) and one Ni^{2+} ion ($S = 1$) arranged in a ring with antiferromagnetic exchange coupling between adjacent metal centres [30]. Atom colours: Ni, green; Cr, purple; F, yellow; O, red; C, grey; hydrogen atoms are omitted for clarity.

evident from the spectrum, for $B_z = 0$ to 8000 G, the ground state and first excited state of the system ($S = 3/2$) are well isolated both from each other and from other excited states.

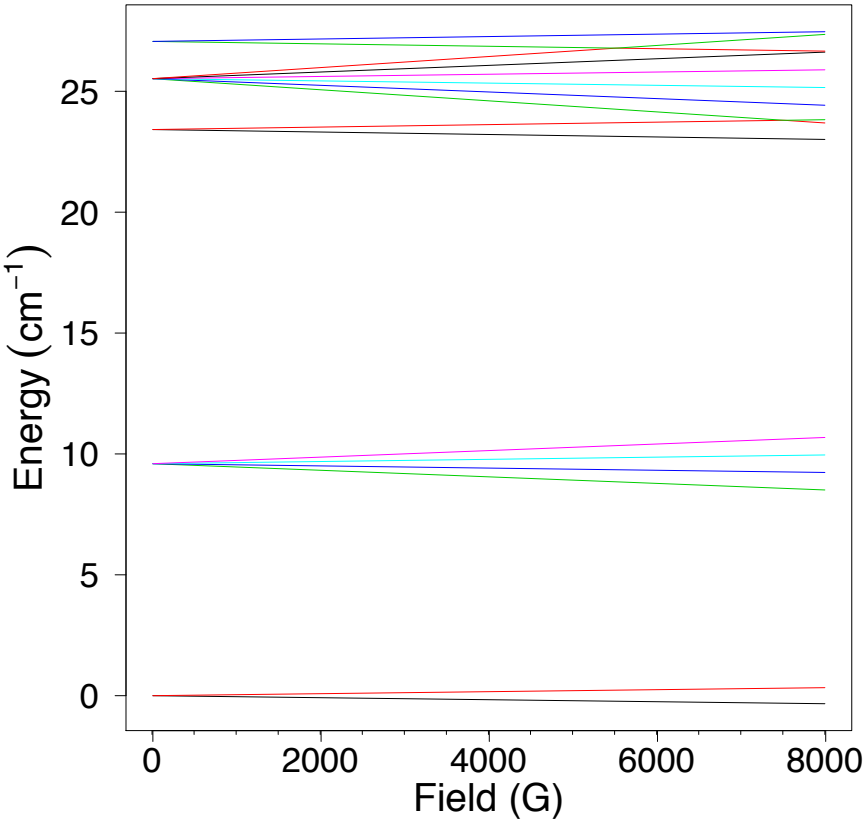

Figure 4.2: The magnetic energy spectrum of $Cr_7Ni-eth$ simulated using the coupling single-ion Hamiltonian from $B_z = 0$ to 8000 G. The energies of the lowest-lying sixteen eigenstates of the system are plotted.

4.3 The CW-ESR spectrum of Cr_7Ni-eth

CW-ESR can be a useful technique for probing the magnetic energy spectrum of a system, and can be used to elucidate many of the parameters contained within the spin Hamiltonian. The CW-ESR spectra plotted in this thesis were recorded using a Bruker EMXmicro spectrometer from room temperature to ~ 4 K. The intensities of all the spectra are in arbitrary units and thus have been normalized. An offset has also been applied to set the baseline to zero intensity. Multiple forms of Cr_7Ni-eth were studied, including a crystalline sample, as well as frozen solutions in toluene of the two synthesized variations of the molecule (Cr_7Ni-eth and Cr_7Ni-eth (p)). The crystalline sample was cut from a twinned crystal of the diethylamine variation of the nanomagnet.

Figure 4.3 illustrates the dependence of the CW-ESR spectrum on temperature for a crystalline sample of Cr_7Ni-eth.

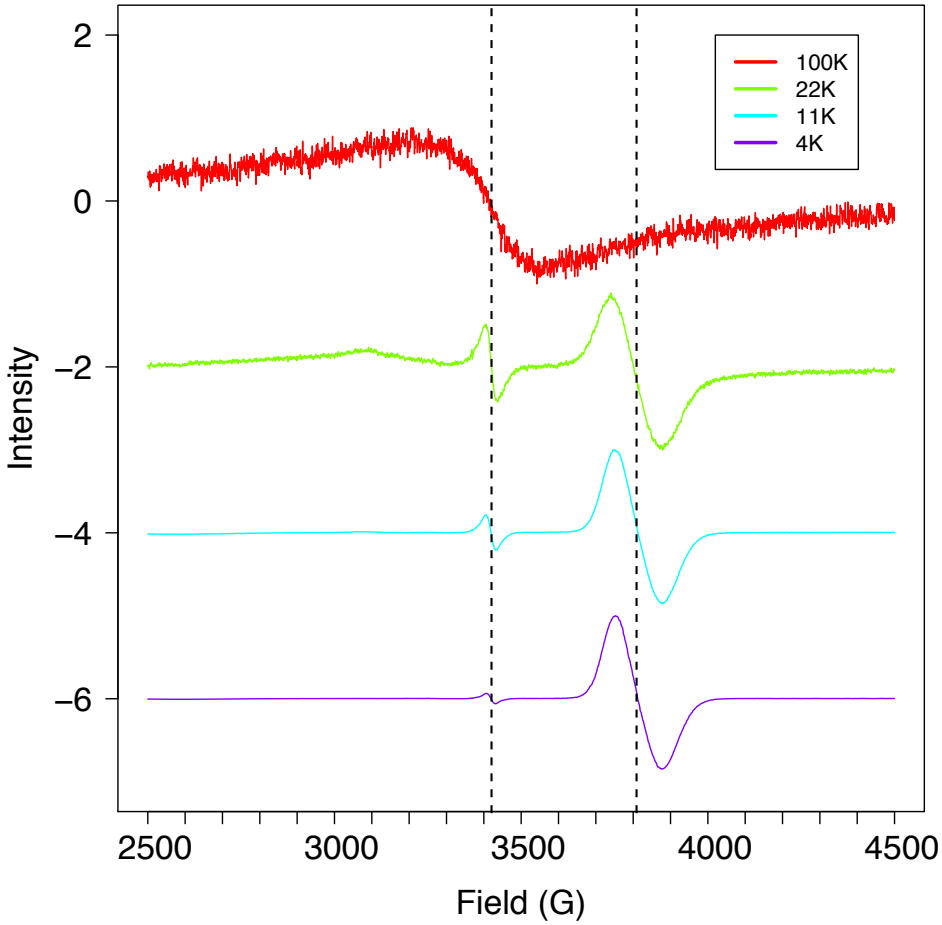

Figure 4.3: The CW-ESR spectrum of polycrystalline Cr_7Ni-eth at (a) 100K (b) 22K (c) 11K and (d) 4K. The spectra have been normalized and offset for clarity. There are two resonances in each of the spectra corresponding to $g = 1.770$ and $g = 1.975$.

The spectra were recorded at 100K, 22K, 11K, and 4K. The spectra measured at 22K, 11K and 4K all display two prominent peaks at $g = 1.770$ and $g = 1.975$. As the temperature is increased from 4K to 22K the intensity of the $g = 1.975$ peak increases relative to the intensity of the larger $g = 1.770$ peak. At higher temperatures the signal widens considerably, becoming only a single broad, weak peak at 100 K.

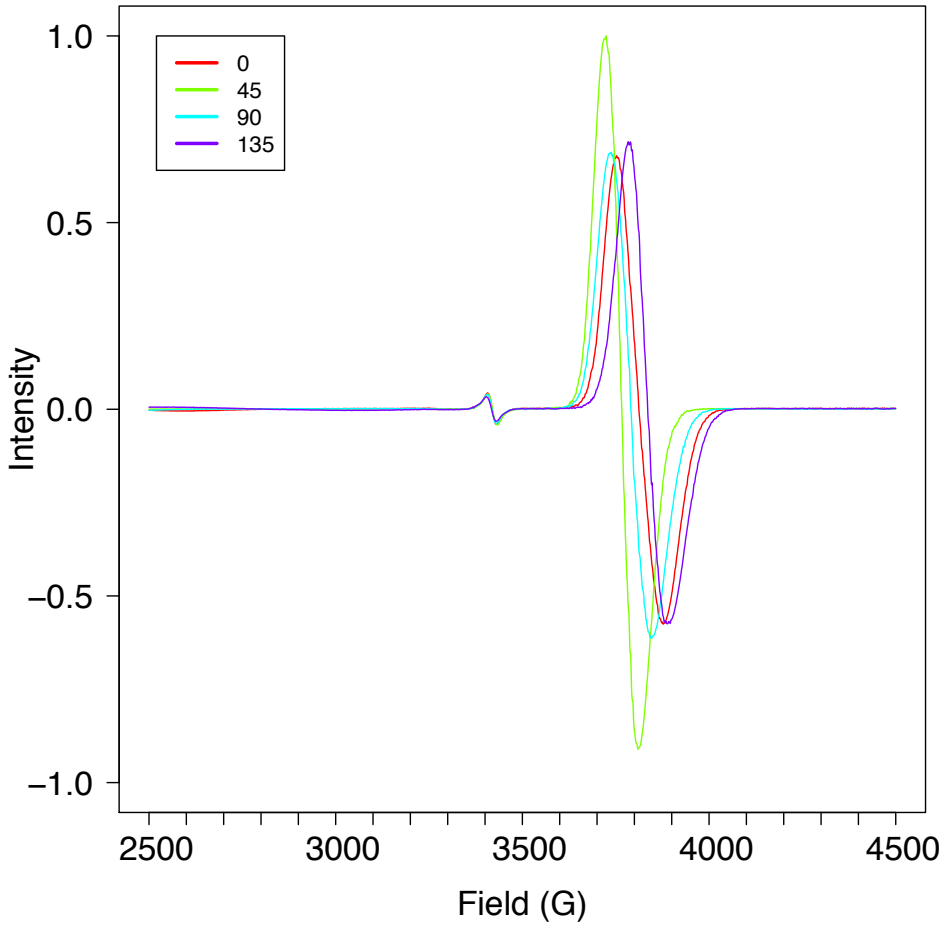

Figure 4.4: The CW-ESR spectra of polycrystalline Cr_7Ni−eth at various orientations of the sample. The spectra were recorded at 4K.

The CW-ESR spectrum of the crystal was also recorded at various orientations of the sample. The shifting of the peak at $g = 1.770$ as the sample is rotated potentially indicates the presence of anisotropy in the system.

Figure 4.5 shows the CW-ESR spectra of frozen solutions of the two synthesized variations of the Cr_7Ni−eth wheel measured at a temperature of 4K. The concentration of both solutions was 3×10^{-5} M. The solutions were prepared in toluene. Given that for both species the magnetic core of the molecule remains the same, one would expect that the CW-ESR spectra of the two compounds would also be similar. Both spectra exhibit the same peaks characteristic of the crystalline sample. There is also a very large, sharp resonance around $g = 2$ that likely corresponds to free organic radicals in the solution. In both spectra the peak around $g = 1.78$ is wider compared to the corresponding peak in the crystalline spectrum, with a full width at half max (FWHM) of 87 G compared to a FWHM of 75 G. This broadening is further evidence of anisotropy in the molecule as the presence of anisotropy will

cause a broadening of the CW-ESR spectrum of a frozen solution.

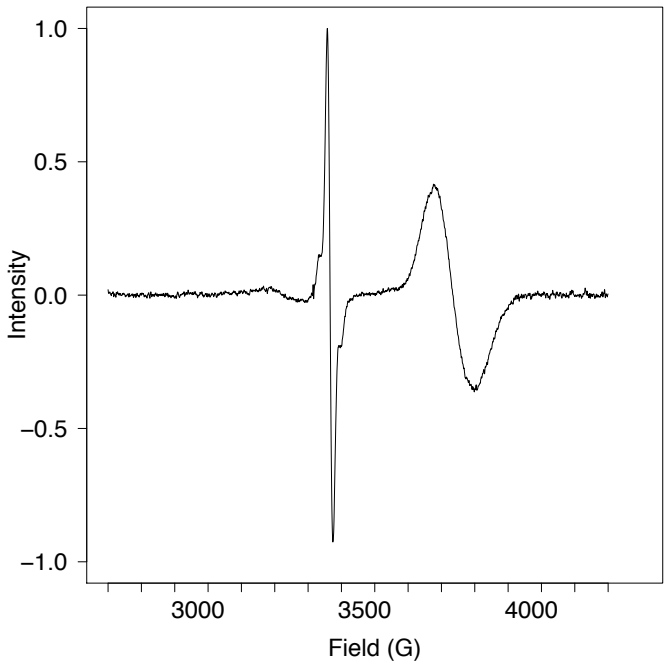

(a)

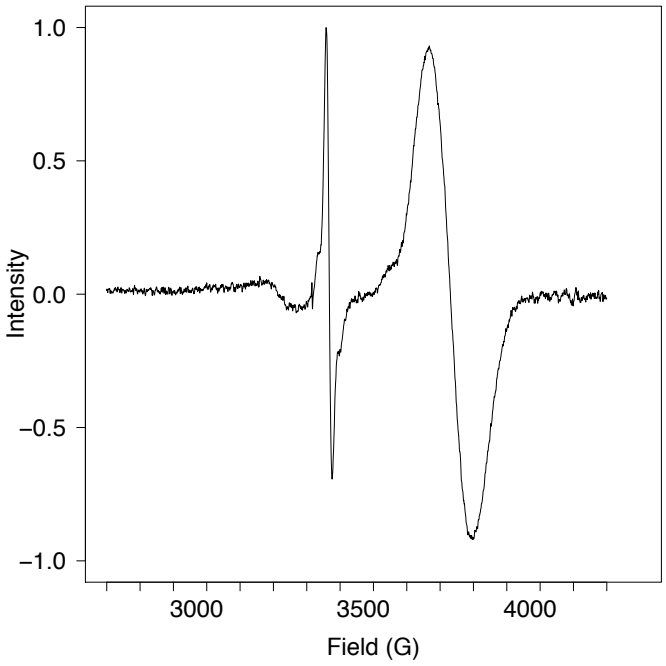

(b)

Figure 4.5: The ESR spectra of frozen solutions of two variations of Cr_7Ni−eth at 4K (a) diethylamine (b) dipropylamine

4.3.1 Simulated CW-ESR spectra

As discussed above, as a first approximation, the isotropic coupling single-ion Hamiltonian, given again in (4.8), was used to simulate the CW-ESR spectrum of the $Cr_7Ni-eth$ wheel.

$$\hat{\mathcal{H}}_{iso} = -2 \sum_{i,j=i+1}^{N} \hat{S}_i J_{ij} \hat{S}_j + \sum_i g_{iso,i} B_z \mu_B \hat{S}_{z,i} \tag{4.8}$$

From the calculated energy spectrum, the transitions that are resonant with the microwave frequency of the CW-ESR experiments were determined (Figure 4.6). The blue arrows in Figure 4.6 denote an expected ESR transition, while the dashed orange lines indicate the value of the applied magnetic field corresponding to the transition. Peaks corresponding to these transitions were then plotted as the first derivatives of Lorentzian curves centred at the magnetic field locations of each transition. Although the widths of the peaks are not directly accounted for, the relative intensities of the signals present in the spectrum are scaled based on the Boltzmann populations of the states involved in each transition. The simulated CW-ESR spectrum at 4K is given in Figure 4.7. At 4K only the transitions in the ground state and first excited state of the system are visible. These peaks occur at $g = 1.78$ and $g = 1.94$.

4.4 Discussion

We applied the isotropic single-ion Hamiltonian to simulate the ESR spectrum of the Cr_7Ni-eth molecular nanomagnet. The calculated positions of the resonances were found to be $g = 1.78$ and $g = 1.94$, while experimental data of a crystalline sample at 4K measured resonances at $g = 1.770$ and $g = 1.975$. Though these values are not in complete agreement the single-ion Hamiltonian was able to replicate the main features of the spectrum. The two resonances at 4 K correspond to transitions in the simulated magnetic energy spectrum in the ground state doublet and the first excited state of the system. As the temperature was increased the relative intensity of these resonances decreased in magnitude as the states corresponding to the transition in the excited state became more populated. Furthermore, at 22 K one begins to see the appearance of a third resonance at a higher g-factor which corresponds to transitions in even higher excited states of the system. The measured CW-ESR spectra of a crystalline sample of Cr_7Ni-eth at different orientations indicate the presence of anisotropy in the sample. Future work will need to be done to understand the anisotropy present in the system, and how to include these effects in the spin Hamiltonian.

Based on the results obtained for the simulated magnetic energy spectrum of Cr_7Ni-eth one is able to gain a greater understanding of the magnetic properties of the nanomagnet. This understanding will be useful for interpreting the results of

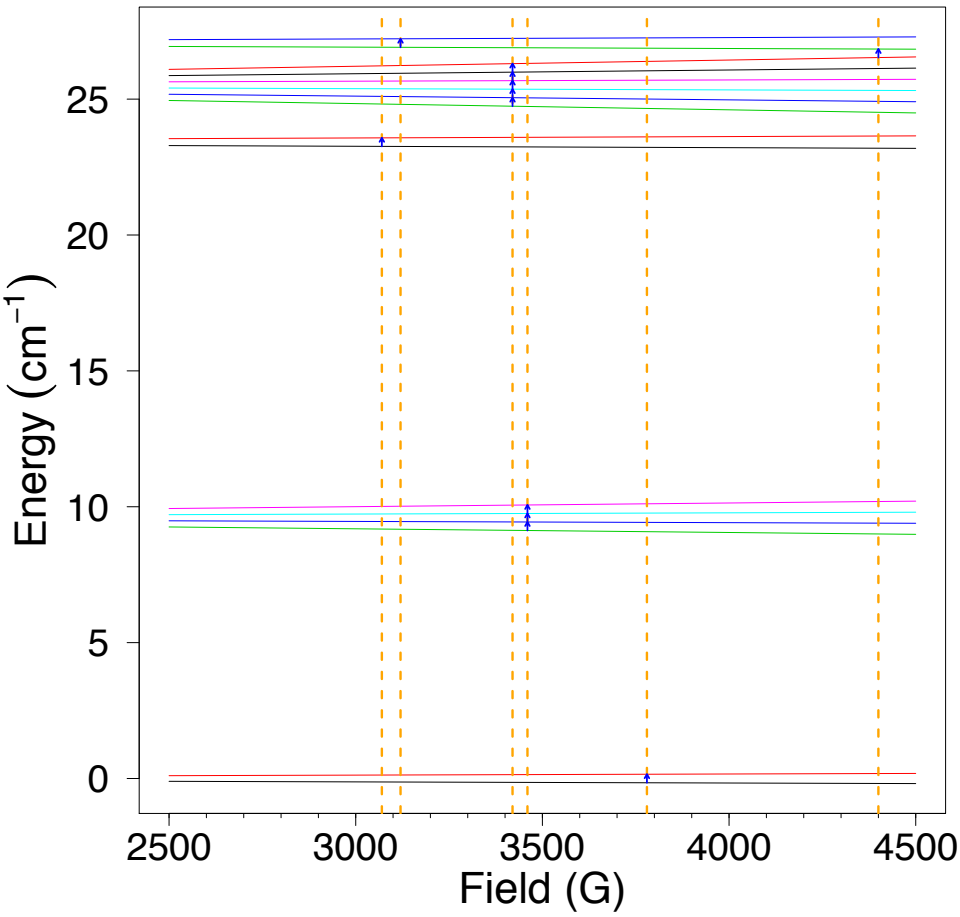

Figure 4.6: The simulated ESR spectrum of $Cr_7Ni-eth$. The expected transitions are determined for a microwave frequency of 9.4 GHz. Transitions between two states are marked with a black arrow. Vertical dashed red lines indicate the values of the applied magnetic field at which the transitions occur.

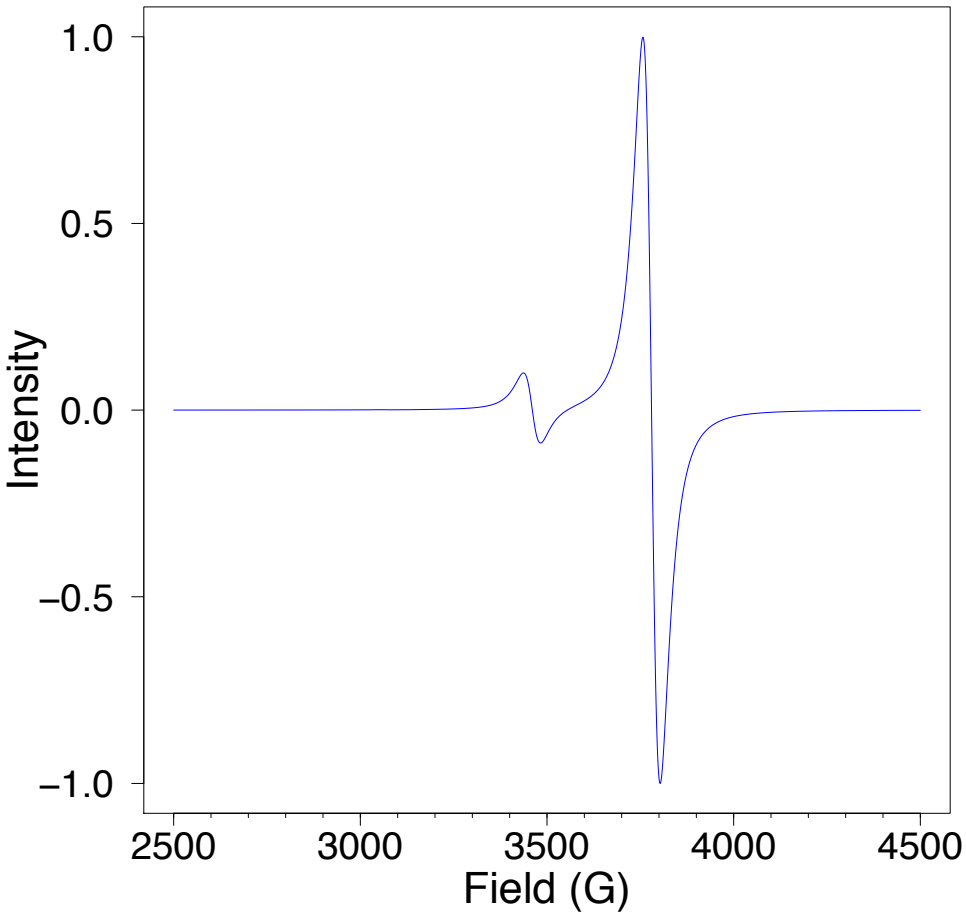

Figure 4.7: The simulated CW-ESR spectrum of $Cr_7Ni-eth$ at 4K. There are two resonances in the spectrum corresponding to $g = 1.78$ and $g = 1.94$. The FWHM of each peak was set to 80 G.

future quantum transport experiments of spintronics devices that contain this molecular system. For example, for the carbon nanotube (CNT) nanoelectromechanical resonator device designed to measure the spin flip of the Cr_7Ni-eth wheel deposited on the CNT [85] (see Section 5.1.2), the transition measured would correspond to the ground state doublet transition at $g = 1.770$.

In addition to further study of the Cr_7Ni-eth system, future work will also include measuring the CW-ESR spectra of the fluorescent Mn_3 SMMs introduced in Chapter 3 of this thesis, with the ultimate goal of extracting the spin Hamiltonian parameters from this data. An initial attempt to simulate the magnetic energy spectrum of these SMMs is discussed below. The fluorescent Mn_3 systems are interesting in part because they contain fluorescent organic ligands. By irradiating a sample of such a Mn_3 nanomagnet with ultraviolet light photoexcited triplet states can be created. Under the right experimental conditions it could be possible to probe the interactions between these states and the magnetic core of the SMM using CW-ESR.

4.4.1 Fluorescent single-molecule magnets

For the purposes of illustrating how the single-ion Hamiltonian and the GSA Hamiltonian can be applied to another magnetic system, we will consider the fluorescent Mn_3 SMMs discussed in Chapter 3 of this thesis. The free parameters in the purely isotropic Hamiltonian given in 4.8 are the exchange couplings J_{ij} and the isotropic g-factors. Considering all of the metal centres in the fluorescent SMMs are identical it is reasonable to assume all of the g-factors and exchange terms will also be equivalent. From previously conducted magnetic susceptibility experiments [65], the g-factor was fit to $g = 1.92$. Given the relatively small size of the magnetic cluster in the Mn_3 SMMs the dimensions of the system would readily permit for the single-ion Hamiltonian to be diagonalized computationally. Consequently, after obtaining experimental CW-ESR data of the molecule, the exchange parameter J could then be varied to fit the measured spectrum.

Although future work will include measuring the experimental CW-ESR spectra of the Mn_3 SMMs, as a first approximation to simulating the magnetic energy spectrum of these compounds the GSA Hamiltonian can be utilized. Applying the GSA and using the value for the anisotropic parameter D fit from magnetic susceptibility data of similar SMMs containing the same magnetic core but with different, non-fluorescent organic shell ligands [65], yields the effective Hamiltonian

$$\begin{aligned}\hat{\mathcal{H}}_{GSA} &= D\hat{S}_z^2 + g\mu_B B_z \hat{S}_z \\ &= (-0.34\ \text{cm}^{-1}) \times \hat{S}_z^2 + g\mu_B B_z \hat{S}_z\end{aligned}$$

The exchange coupling between the Mn ions in the core of the fluorescent Mn_3 SMMs is weaker compared to what was measured for the similar SMMs containing non-fluorescent ligands. Consequently it is expected that mixing could occur between the ground state of the system and low-lying excited states [2], violating

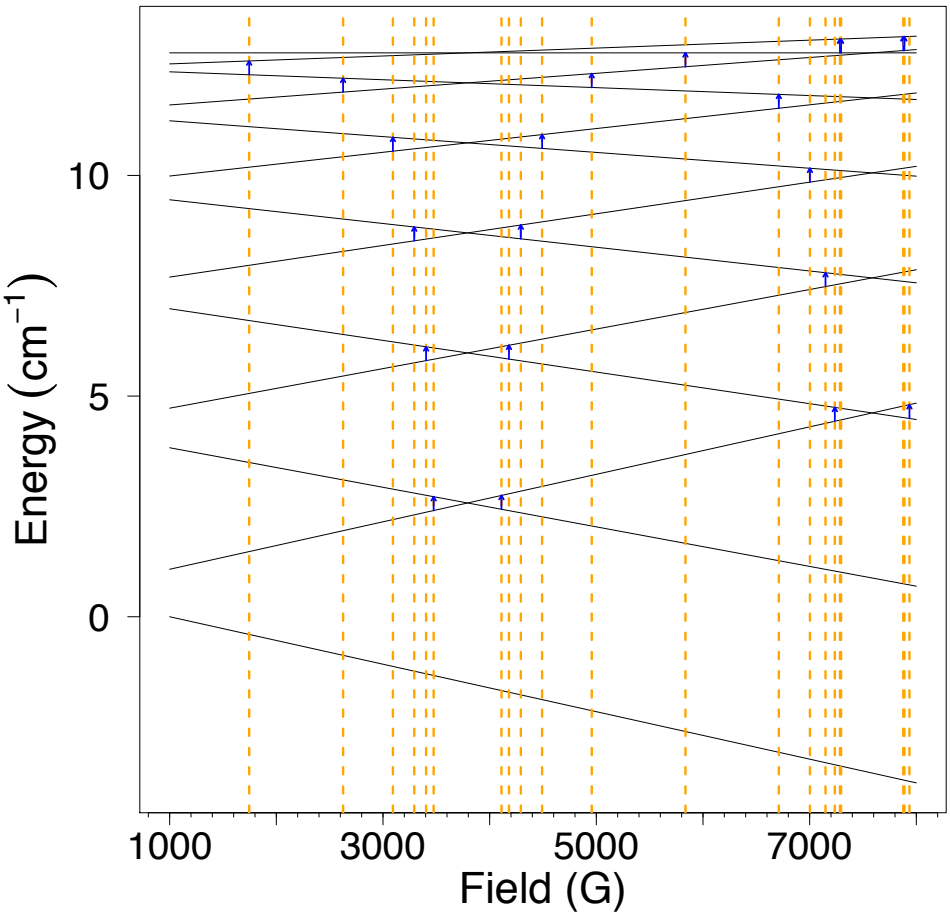

Figure 4.8: The calculated ESR frequencies of the Mn_3 SMM. The expected transitions are determined for a microwave frequency of 9.395 GHz. Transitions between two states are marked with a blue arrow. Vertical dashed red lines indicate the values of the applied magnetic field at which the transitions occur.

the conditions of the GSA. Despite this result, utilizing the GSA Hamiltonian can provide a first approximation for what to expect from the experimental CW-ESR spectra of the Mn_3 SMMs. Diagonalizing the Hamiltonian and finding the calculated ESR frequencies yields the plot in Figure 4.8. The simulated ESR spectrum is then given in Figure 4.9. Although this result is just an approximation of the expected spectrum of the Mn_3 SMMs, it illustrates how the program we created in MATLAB can be applied to different species of molecular nanomagnets.

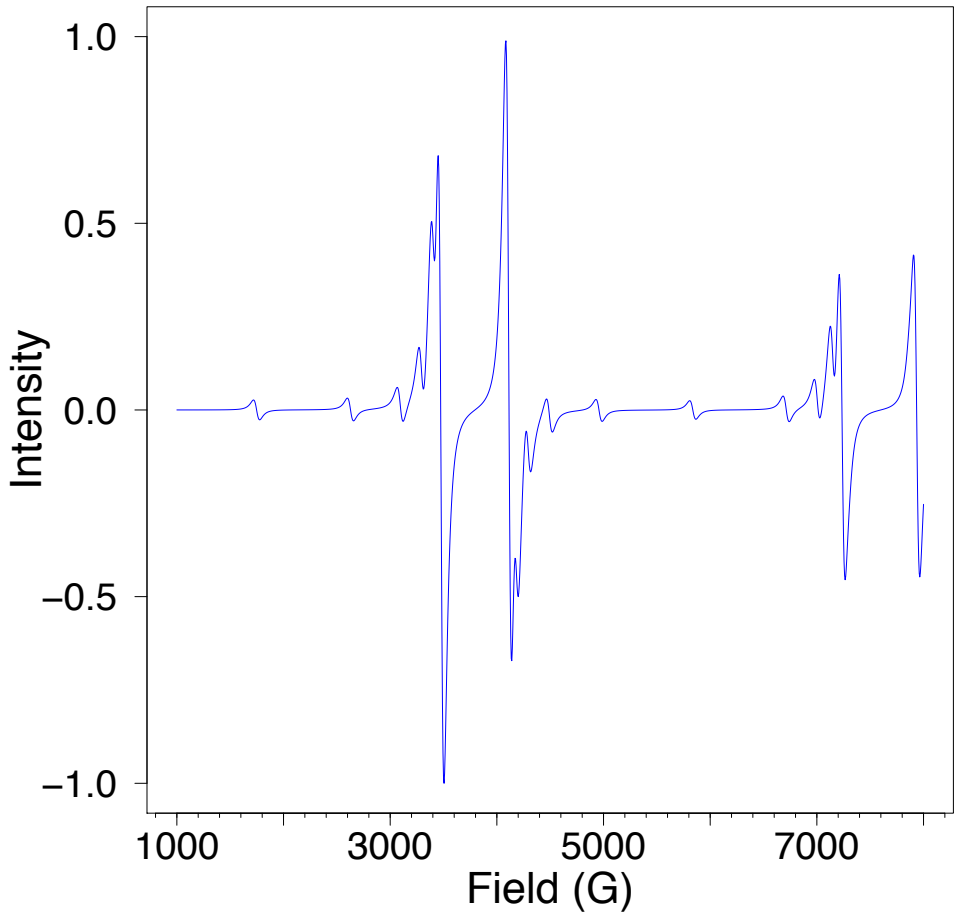

Figure 4.9: The simulated ESR spectrum of the Mn_3 SMM at 4 K. The FWHM for each peak was set to 100 G.

Chapter 5

Toward novel molecular spintronic devices

Chapter 5 of this thesis discusses a series of experiments conducted in order to develop a process for studying the properties of molecular nanomagnets attached to graphene surfaces. The first steps of this process involve obtaining clean graphene flakes on which to deposit the molecules of interest. Atomic force microscopy (AFM) and Raman spectroscopy are used to categorize both the quality of the graphene flakes, as well as to analyze the results of molecular depositions.

5.1 Introduction

Molecular electronics concerns the incorporation of molecular elements into nanoelectronic devices. Molecular spintronics is a field of study within molecular electronics where the molecular systems of interest are molecular nanomagnets [9, 26]. The purposes of the fabricated devices vary from attempting to gain a greater understanding of the properties of the integrated molecular systems to analyzing the potential viability of these systems in modern technological applications such as quantum computing. The behaviour of the devices will depend on the individual properties of both the molecular and the nanoelectronic components, as well as the coupling between the two systems.

A variety of devices have been proposed and realized in the field of molecular spintronics [9, 26, 58]. The geometries and nature of the devices can be classified based on whether electric current directly flows through the molecular component, or whether the molecular compound is coupled to a conducting element through which the current flows. In both cases the transport characteristics of the device will be dependent on the properties of the integrated molecule in some fashion. An example of a directly coupled geometry is a molecular transistor [58], while an example of a device that employs an indirect scheme is a carbon nanotube nanoelectromechanical resonator coupled to a single-molecule magnet (SMM) [85, 24].

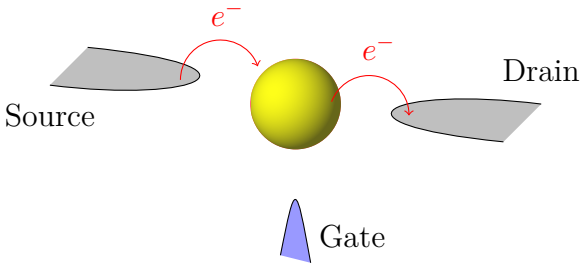

Figure 5.1: Schematic of a molecular transistor. A molecular transistor is a three terminal device consisting of a molecular system connected to source and drain electrodes and capacitively coupled to a gate electrode. Electrons can tunnel from the source electrode to the molecule, and from to the molecule to the drain.

5.1.1 Molecular transistors

A molecular transistor is a three terminal break-gap junction device that consists of two leads connected via a molecule (Figure 5.1). This type of device is commonly fabricated by creating a nanometre sized gap in a gold nanowire, across which a single molecule is deposited. The gap in the nanowire is typically formed using either a controlled electromigration technique [66], or through a mechanical breaking mechanism [15]. Further tuning of the transistor is accomplished by applying a gate voltage to a gate electrode that is capacitively coupled to the molecular system. Transport across the molecule will occur when the energy of a molecular orbital is in resonance with occupied electronic levels in the leads. Molecular transistors have been used as a spectroscopic tool, relating transport characteristics to the electronic structure of the integrated molecules, and in the field of molecular spintronics as a test bed for experimentally manipulating the spin of a SMM (see Figure 5.2) [63, 69, 57].

Dithiols are examples of purely organic molecules that have been extensively studied through transport experiments of break-gap junction devices [64, 63, 44]. These molecules contain terminating thiol ligands that will covalently bond to the gold electrodes in a device, anchoring the molecular system to the leads. Depending on the chemical structure of the dithiol being investigated, the molecule will either behave as an insulator, with transport properties similar to that of a quantum dot, or as a conducting molecular wire. A range of dithiols have been studied, including dithiols with a saturated alkyl backbone, and dithiols containing extended, delocalized π-systems of electrons. In addition to studying the conductance properties of these systems, using a three terminal, single-molecule transistor geometry, the vibrational spectra of these compounds have also been probed [64, 63].

As discussed in Chapter 3 of this thesis, the organic shell of molecular nanomagnets can be functionalized using well known methods of organic synthesis. By selecting specific functional groups to bond to the magnetic core of the nanomagnet, the coupling of the molecule to its environment can be explicitly tailored for a desired

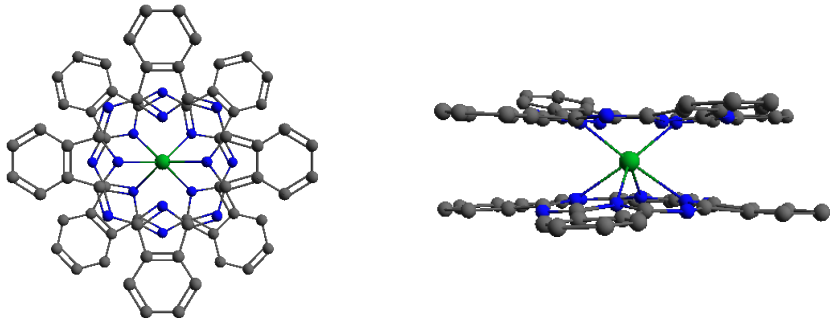

Figure 5.2: The chemical structure of a *bis*-phthalocyaninato-terbium (III) complex ($TbPc_2$). The $TbPc_2$ SMM consists of a single Tb ion sandwiched between two phthalocyaninato ligands. This molecule has been shown to display the typical magnetic properties of an SMM and has been studied extensively in molecular spin transistors due in part to its stability when deposited on a surface. Atom colours: Tb, green; N, blue; C, grey; hydrogen atoms are omitted for clarity [20].

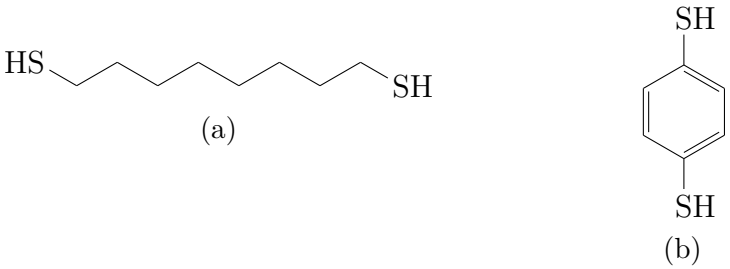

Figure 5.3: The chemical structure of (a) 1,8-octanedithiol and (b) 1,4-benzenedithiol. With a saturated, alkyl backbone, 1,8-octanedithiol will behave as an insulator, while due to the π-conjugation present in 1,4-benzenedithiol, this molecule will exhibit significantly higher conductance.

application. For example, as suggested above, in order to facilitate the formation of covalent bonds between gold electrodes and a molecular nanomagnet, sulfur containing ligands can be incorporated into the nanomagnet's organic shell. A covalently bonded molecule lying across a break-gap junction will exhibit stronger coupling to the leads compared to a system attached to the electrodes through weaker forces. The transport properties of the device will depend on the coupling between the two systems. For example, in the weakly coupled regime charging effects will have the most significant impact on the transport properties; Coulomb diamonds can be observed in a plot of differential conductance as a function of the bias voltage and the gate voltage [9]. The charging of the nanomagnet can affect the magnetic nature of the system, and thus one has to also take into account the properties of the positively charged and negatively charged forms of the molecule. Considering it is possible to experimentally synthesize these charged species, the use of nanomagnets in these devices allows for a direct comparison to be made between the results of common structural and magnetic characterization techniques and transport measurements [33, 35, 14].

5.1.2 Carbon-based molecular nanoelectronics

Carbon nanostructures (i.e. carbon nanotubes (CNTs) and graphene) have also been employed as nanoelectronic components in molecular electronics devices [8, 18, 76, 24]. In devices that utilize carbon-based electronics it is imperative that the molecular component being integrated does not interact significantly with the graphitic structure in order to retain both the magnetic properties of the molecular system, and the transport properties of the carbon nanostructure. As a result strategies have been employed that attempt to exploit forces significantly weaker than covalent bonds: van der Waals forces, and π-π stacking interactions. Understanding the interactions between the molecular and nanoelectronic components is of vital importance when considering the use of carbon-based materials.

Potential devices that incorporate carbon nanostructures include graphene break-gap junctions fabricated using electroburning [40], and a CNT nanoelectromechanical resonator designed to probe the magnetic moment of the molecular system [85, 24]. Previous attempts to couple the magnetic moment of a molecular nanomagnet to the mechanical oscillations of a CNT have been based on torque magnetometry [25, 39, 24]. In this scheme, a magnetic field is applied to a molecular nanomagnet grafted to a CNT causing the magnetic moment of the molecule to rotate. As the magnetic moment changes direction, the molecule itself will rotate to minimize its anisotropic energy. This motion induces tension in the CNT causing a detectable shift in its mechanical resonance frequency [25, 39, 24, 85].

An alternative proposal by Willick et al. (2014) utilizes a suspended CNT resonator and a ferromagnetic gate to detect the magnetic state of a molecular nanomagnet attached to the CNT. By applying a magnetic field gradient to a nanomagnet grafted to a suspended CNT, the resulting force imparted on the tube by

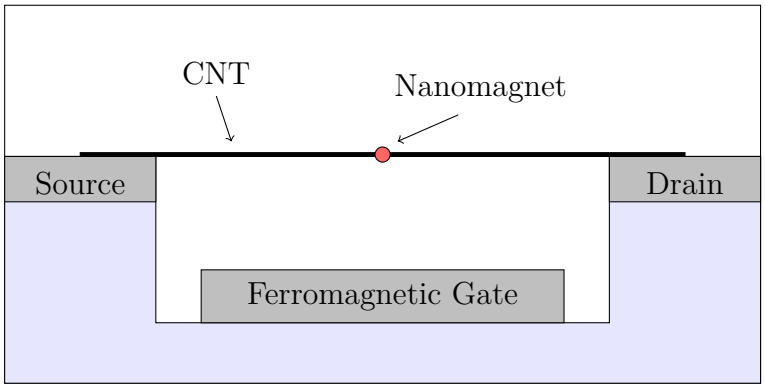

Figure 5.4: Schematic of a carbon nanotube mechanical resonator proposed by Willick et al. (2014) [85]. The force imparted on the nanotube by the response of the nanomagnet to the ferromagnetic gate will affect the mechanical resonance of the CNT (see Section 5.1.2). Figure adapted from [84].

the magnetic response of the molecular system to the field will cause a significant, measurable shift in the nanomechanical resonance of the device [85]. This shift in resonance frequency would allow for the detection of the magnetic reversal of the nanomagnet as well as electron spin resonance under microwave excitation [85].

5.1.3 The characterization of molecular nanomagnets on a surface

Studying the properties of molecular nanomagnets deposited on a surface can help shed some light on the nature of the interactions between the molecular and nanoelectronic components of a molecular spintronics device. Furthermore, confirming which molecular nanomagnets retain their chemical and magnetic stability when deposited on a surface is integral in guiding the selection of the molecular system to be incorporated into a proposed device geometry. In general, the properties of molecular nanomagnets assembled on a surface may vary considerably compared to those of the same molecule in crystalline form. For example, it was determined that a significant number of the manganese ions in the Mn_{12}-acetate SMM were reduced to Mn^{2+} from Mn^{3+} when the molecule was deposited on a gold surface [49].

Various complementary experimental techniques have been employed for studying assemblies of molecular nanomagnets on a surface. Scanning probe techniques, such as AFM, can be used to image the surface topography of layers of the nanomagnets, and under the right experimental conditions, scanning tunnelling microscopy (STM) can be utilized to visualize a molecule on a surface at the single-molecule level [78, 60]. Mass spectrometry has been used to compare the fragment patterns of both a crystalline SMM, and a monolayer of the same molecules, to verify the structural stability of the compound on a surface [60]. Similarly, Raman spectroscopy has also been used to confirm that the vibrational modes of functional groups present in

a system do not vary between the free molecule and the deposited molecule [47]. X-ray photoelectron spectroscopy (XPS) [60] and x-ray absorption spectroscopy (XAS) have been used to obtain quantitative structural information concerning the chemical composition of deposited molecules, and the oxidation states of the constituent metal ions [49]. The magnetic properties of a nanomagnet deposited on a surface can be studied using micro-SQUIDS (superconducting quantum interference devices) [18], and x-ray magnetic circular dichroism (XMCD) [49]. Utilizing combinations of these techniques, the chemical and magnetic stability of a specific nanomagnets deposited on a surface can be analyzed.

5.2 Binding studies

We have conducted a series of experiments to develop a procedure for studying the chemical and magnetic stability of a variety of molecular nanomagnets on graphene substrates. The molecular nanomagnets studied include the synthesized variant of the Cr_7Ni family of antiferromagnetic wheels discussed in Chapter 3 of this thesis (Cr_7Ni-eth), as well as the Mn_3 nanomagnets obtained through collaborations with other research groups [65, 2]. The ultimate goal of these studies is to determine the viability of these magnetic systems for use in molecular transistors, and as the molecular component in a carbon nanotube nanoelectromechanical resonator device. By categorizing the interactions between the nanomagnets and the graphene substrate we hope to gain a better understanding for how the molecule will behave when integrated into these nanoelectronic devices.

5.2.1 Preparation of graphene substrates

In order to systematically study the binding of molecular nanomagnets to graphene, consistent, reliable, graphene surfaces must be produced. The graphene needs to be pristine, in the sense that it must be resting flat enough with clear edges, and be sufficiently clean, in order to discern the presence of nanometre sized particles on its surface. The graphene samples were analyzed using AFM and Raman spectroscopy. AFM images were obtained with a Digital Instruments Multimode^{TM} Atomic Force Microscope operated in tapping mode with a silicon tip, and the Raman spectra were acquired using a Horiba Jobin Yvon HR800 Raman spectrometer equipped with three laser light sources at 532.06 nm, 632.817 nm, and 785.83 nm and an Olympus BX41 microscope. Initially, the graphene flakes were prepared by reducing graphene oxide (GO) that had been deposited on mica. Freshly cleaved mica has an exceptionally flat surface making it an ideal substrate for AFM.

Reduced graphene oxide

The process followed for preparing monolayer graphene sheets from GO was as follows:

1. Synthesize GO following Hummers method [34, 27].

2. Drop-cast a solution of GO dispersed in a 1:1 ethanol to water mixture on mica. The solution is diluted from a stock solution with an approximate concentration of 5 mg/mL until the colour of the diluted solution is a light yellow ($\sim$ 0.25 mg/mL). Add three drops of the diluted solution to the mica substrate, allow to sit for approximately five minutes and then blow the surface of the sample dry with nitrogen.

3. Place the mica samples, along with hydrazine, in a sealed vessel on a hot plate to expose the GO to a hydrazine environment. In the presence of the hydrazine the GO will be reduced to monolayer graphene. Reduction of GO to graphene can be confirmed through ultraviolet-visible (UV-Vis) absorption spectroscopy. The absorbance spectrum of reduced GO can be distinguished from that of GO.

The quality of the monolayer graphene flakes produced using this method seemed in part to depend on the length of time the GO sample was exposed to the hydrazine environment. Initially the GO was reduced for a period of eight hours. However, it was observed that the longer the GO was exposed, the worse the quality of the flakes appeared, and the smaller the number of flakes that remained on the mica substrate. Consequently, subsequent reductions were done over approximately four hours, until the edges of the sample turned a dark colour. After the GO solution was drop-cast and allowed to sit, the solvent was evaporated by blowing it dry with nitrogen. As the solvent evaporated a concentrated ring of GO would form around the edges of the mica sample. After the reduction of the GO, this ring would turn a darker colour, providing an indication for when the sample can be removed from the hydrazine environment. A sample of the AFM images illustrating the graphene flakes produced through the reduction of GO on mica are given in Figure 5.5.[1]

Mechanically Exfoliated Graphene

While on occasion the reduction of GO to obtain clean graphene substrates was successful, the results were variable, depending primarily on the initial quality of the GO sample, and the length of time the reduction was performed. However, even when all of the conditions were kept consistent, the graphene flakes produced still had a wide variation in quality. Consequently, in order to obtain more consistent flakes to perform depositions on, we switched our focus to the "scotch tape" method of mechanical exfoliation [56]. We strived to produce reasonably large flakes that would be suitable to image submonolayer depositions of molecular nanomagnets.

[1] All AFM images were processed and displayed using the open-source software package Gwyddion [53]

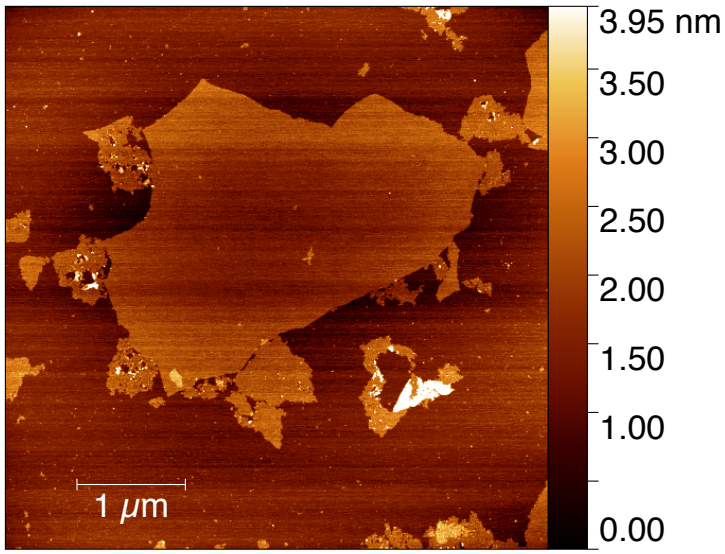

(a)

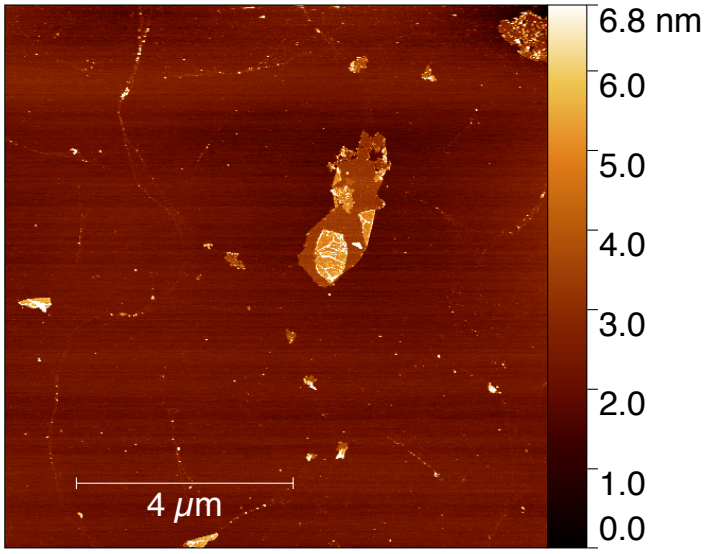

(b)

Figure 5.5: The variation in the quality of reduced GO deposited on mica. The concentration of the deposited GO solution was approximately 0.25 mg/mL.

The general procedure followed for the mechanical exfoliation of graphite is given below. Natural Kish graphite (grade 300) purchased from the Graphene Supermarket was used to produce the graphene flakes.

1. Place a piece of graphite on a piece of adhesive tape. Work the graphite by continuously attaching the ends of the tape together and then pulling them apart.

2. Once a layer of worked graphite remains on the tape, press the tape to a silicon substrate with a 300 nm layer of silicon dioxide. This specific thickness of oxide growth is necessary for creating the contrast required to optically locate the graphene flakes.

3. Locate suitable monolayer or bilayer flakes using an optical microscope. A suitable flake is one that does not appear to contain many folds on its surface.

4. Characterize the flakes using Raman spectroscopy and atomic force microscopy. The number of layers present in the sample can be conclusively determined based on the Raman spectrum of the flake, while the roughness, and cleanliness of the flake can be determined via AFM.

The flakes that were selected for further study were commonly either bilayer or monolayer graphene. The flakes were of good quality but typically were contaminated with some form of residue, potentially due to the adhesive tape used in the exfoliation process (Figure 5.7 (a)). In order to successfully image deposited molecular nanomagnets on the surface of the graphene, this residue was required to be cleaned.

The typical Raman spectra of monolayer, bilayer, and multilayer graphene are shown in Figure 5.6.The presence of additional layers causes a change in the ratio of the intensities of the 2D peak (at approximately 2680 cm^{-1}) to the G peak ($\sim$ 1580 cm^{-1}) in the spectrum. As well, the 2D peak in monolayer graphene is sharper, and shifted to a lower wavenumber, compared to the same peak in multilayer graphene [21].

Three strategies were attempted to clean the residue present on the exfoliated graphene flakes. The success of each strategy was measured based on whether the graphene flake appeared more clean while still retaining the same characteristic Raman spectrum. Each technique is described in the following sections.

Organic solvent rinse

The dirty flakes were submerged in an organic solvent (either chloroform or acetone) for a few minutes, and gently agitated in an attempt to dissolve the residues. If the flake was subjected to too large an amount of agitation (i.e. extended periods of ultrasonication) there would be a risk of removing the graphene flake from the substrate. After soaking the flake in the solvent, the substrate was removed and

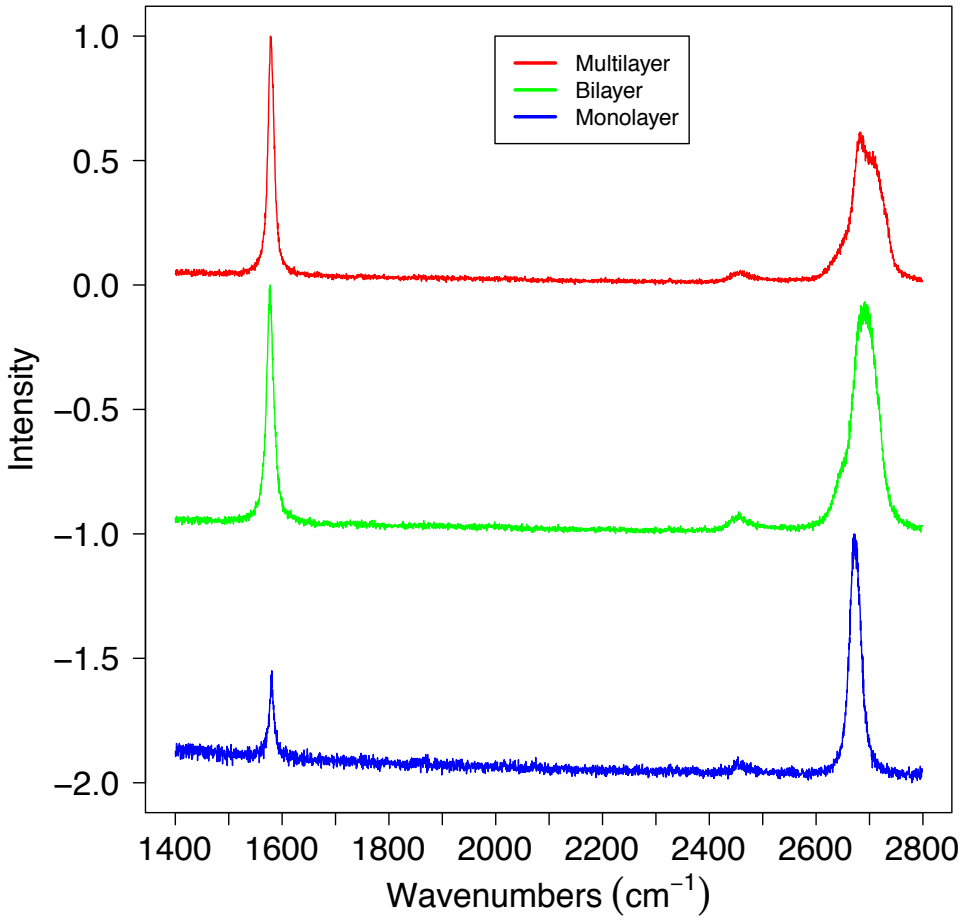

Figure 5.6: The Raman spectra of multilayer, bilayer and monolayer graphene. In monolayer graphene the ratio of the 2D peak ($\sim$ 2680 cm^{-1}) to the G peak ($\sim$ 1580 cm^{-1}) is close to 2:1. For bilayer graphene the ratio of the two peaks is 1:1, and when more layers are present the G peak becomes more intense than the 2D peak.

transferred to a vial of isopropanol to remove any additional residues left from the solvent rinse. The substrate was then blown-dry with nitrogen (see Figure 5.8 (a) and (b)).

Annealing

The flakes were annealed at 400°C under an inert atmosphere for different periods of time (Figure 5.7).

Remover PG rinse

The substrate was immersed in a beaker of remover PG and then rinsed with acetone and isopropanol before being blown-dry with nitrogen gas. Remover PG is a proprietary solvent mixture made by MicroChem containing primarily N-methyl-2-pyrrilidone that is commonly used to remove photoresist during lithographic processes.

5.2.2 Molecular nanomagnet deposition

When a flake was identified as suitable for deposition, the substrate containing the flake was placed in a solution of a molecular nanomagnet and allowed to sit overnight. For initial deposition tests the molecular nanomagnets were dissolved in chloroform with a concentration of $\sim 10^{-4}$M. Upon removal from the solution, the substrate was washed in clean chloroform and then rinsed in water, in an attempt to remove any residues left behind on the mica substrate by the organic solvent.

5.2.3 Discussion

As outlined above, initially graphene flakes were produced by reducing GO deposited on mica. Although mica is exceptionally flat, and thus a good substrate to use for AFM imaging, due to its fragility once a specific mica substrate had been affixed to an AFM sample holder, it could not be removed without destroying the sample. As a result it was not possible to study a particular flake on the surface of the mica prior to performing a molecular deposition. Furthermore, the GO was not visible optically when drop-cast on the mica substrate. Consequently, it was also not possible to obtain the Raman spectrum of a specific flake. Both of these technical issues could potentially be remedied by using Si/SiO_2 as a substrate, but GO does not adhere to silicon dioxide particularly well.

Despite these problems, the reduction of GO was still capable of producing flakes suitable to use in a deposition of a molecular nanomagnet. Figure 5.9 illustrates the results of one such deposition, where the Cr_7Ni-eth molecular nanomagnet was deposited on a flake of reduced GO. From this image it appears as though the molecular nanomagnet is potentially showing a preference for bonding to the reduced GO, with a larger number of aggregates of particles conglomerating on the surface of

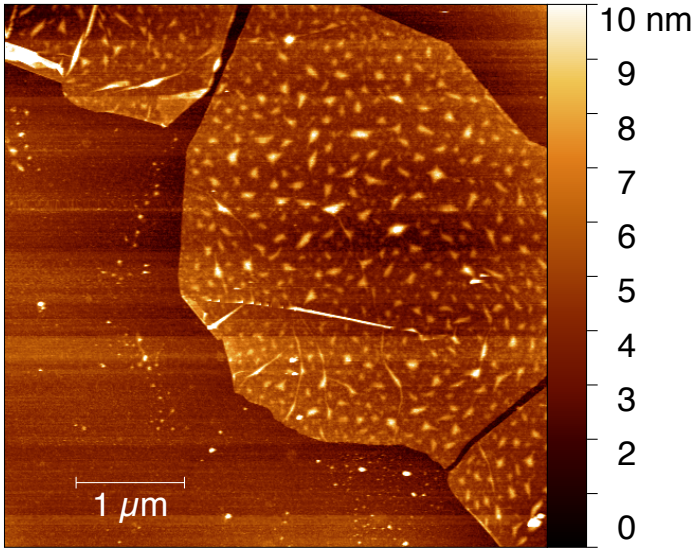

(a) Before annealing

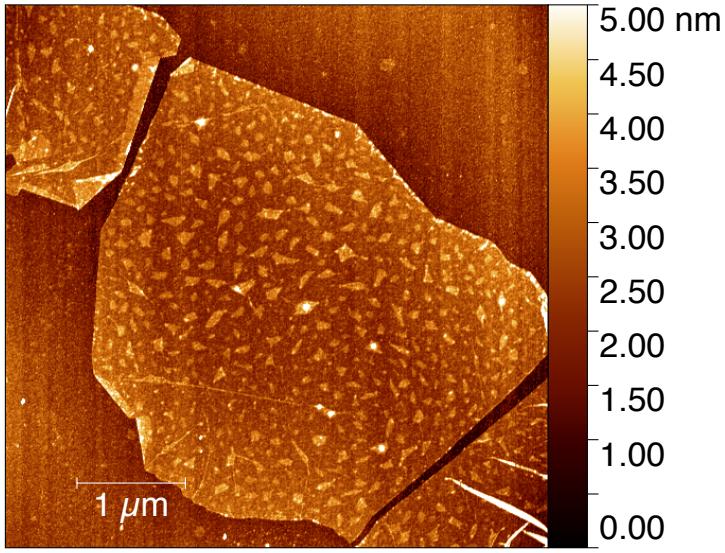

(b) After annealing

Figure 5.7: A graphene flake deposited on Si/SiO_2 cleaned by annealing. (a) The flake before annealing. From the recorded Raman spectrum this flake was identified as bilayer graphene. (b) The flake after annealing at 400°C under an argon atmosphere for approximately 10 minutes initially, followed by a longer period of annealing for 40 minutes. There was no discernible difference between the flake after the first annealing and the flake after the longer period of heating.

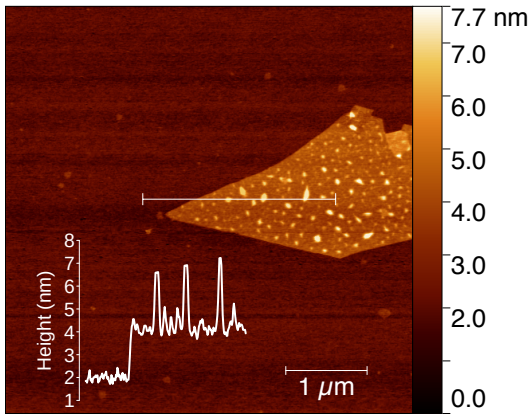

(a) After exfoliation

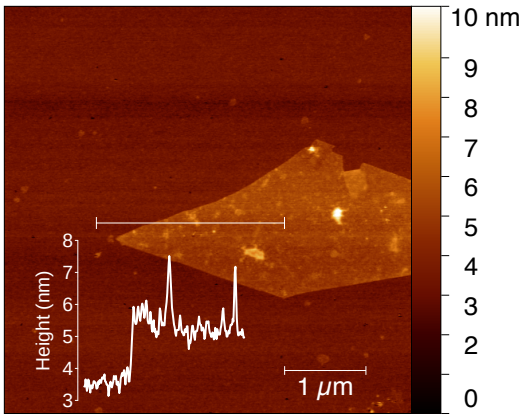

(b) After a solvent rinse

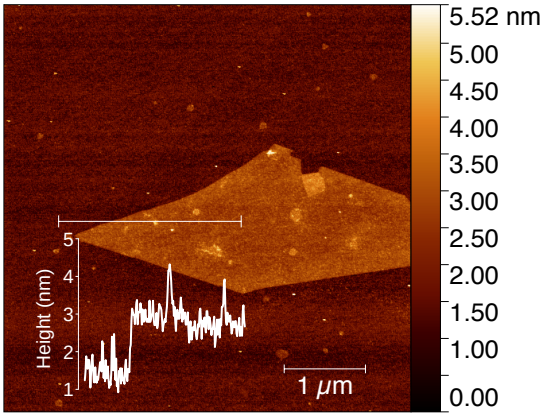

(c) After annealing

Root Mean Square Roughness		
	Flake (nm)	Substrate (nm)
(a)	0.746	0.255
(b)	0.730	0.498
(c)	0.436	0.326

Figure 5.8: AFM images mapping the progress of the cleaning of a graphene flake deposited on Si/SiO_2. (a) A bilayer graphene flake imaged after exfoliation that is covered in residues. The cross-sectional height profile indicates that these residues are approximately 4 nm tall. (b) After rinsing the same bilayer flake in chloroform followed by isopropanol, the height profile taken along the same line as that in (a) shows that many of the residues have been removed. (c) The same flake after being annealed at 400°C in a hydrogen/argon atmosphere (1:4 ratio) for approximately two hours. The surface of the flake is now significantly less rough compared to the flake prior to the cleaning procedure. Annealing the flake has also caused it to sit flatter on the substrate.

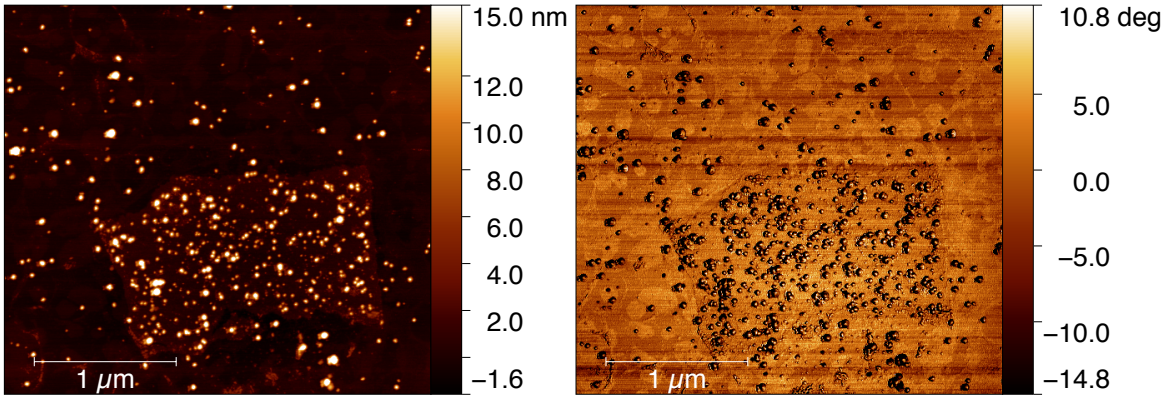

(a) (b)

Figure 5.9: Deposition of Cr_7Ni−eth on reduced GO on mica. The substrate was placed in an approximately 10^{-4}M solution of Cr_7Ni−eth in chloroform overnight. There appeared to be a larger number of molecules deposited on the surface of the reduced GO compared to the substrate. (a) Height data (b) Phase data.

the flake compared to the mica substrate. However, due to the limitations outlined in the preceding paragraph it is difficult to draw any hard conclusions. As a further example, consider Figure 5.10. In this instance, a solution of the Mn_3-pyr SMM was deposited on a sample of reduced GO on mica with a similar concentration to the previous deposition displayed in Figure 5.9. However, due to the poor quality of the flakes on this substrate it is difficult to reach any conclusions regarding the outcome of the deposition. Unfortunately, it was not possible to determine ahead of time whether a particular sample produced by the reduction of GO contained suitable flakes.

As a result our attention shifted to producing graphene flakes using the mechanical exfoliation technique. This technique provided the added benefit of using Si/SiO_2 as a substrate, allowing for before and after studies of a given flake (see Figure 5.11). Using the mechanical exfoliation technique the graphene flakes produced were commonly found to be dirty with residues potentially originating from the adhesive tape used in the method. While each cleaning strategy applied to remove these residues was met with some success, the results varied from sample to sample. The most effective method proved to be a combination of the different cleaning techniques: a solvent rinse followed by an annealing step (Figure 5.8). As evident by the cross-sectional profiles of the graphene flakes displayed in Figure 5.8, with each successive cleaning step the roughness of the flake decreased. The roughness of the flake can be measured by determining the root mean square (RMS) of the deviations of the height of each point from the average height of the flake. The table in Figure 5.8 indicates that with each step of the cleaning process the roughness of the flake decreases. After the annealing step (Figure 5.8 (c)) the ratio of the 2D to the G peak in the Raman spectrum of the flake suggested that the flake was

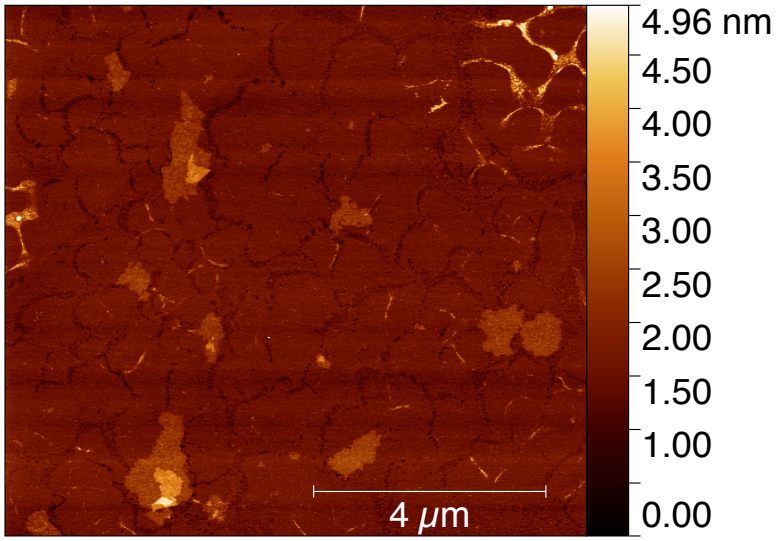

Figure 5.10: Deposition of Mn_3-pyr on reduced GO on mica. The substrate was placed in an approximately 10^{-4} M solution of Mn_3-pyr in chloroform overnight. Due to the lack of quality flakes on the mica surface it is difficult to make any conclusions regarding the deposition.

no longer a bilayer piece of graphene, but rather consisted of multiple layers. The annealing conditions were slightly different compared to what was done previously in that the flake was annealed under a hydrogen/argon atmosphere in a 1:4 ratio, as opposed to solely argon. It is possible that the presence of the hydrogen might have altered the surface of the graphene flake in such a way as to modify the vibrational spectrum of the system. This observation potentially warrants future investigation.

Figure 5.11 illustrates the entire process from the initial exfoliation to a molecular deposition. This flake was not cleaned using the developed method described in the preceding paragraph, but was instead cleaned by first rinsing in remover PG and then in acetone. The remover PG seemed to be harsh on the graphene as the surface of the flake appeared weathered when imaged with AFM after the cleaning procedure. Despite this reaction, Figure 5.11 demonstrates the benefits of utilizing the mechanical exfoliation technique, as the flake can be characterized at each step of the process. The Cr_7Ni-eth nanomagnet was deposited on the flake from a solution in chloroform with a concentration of $\sim 10^{-4}$ M. The cross-sectional profiles indicates a larger increase in the roughness of the graphene flake after the deposition compared to the bare substrate.

The Raman spectrum of the flake depicted in Figure 5.11 was measured after the deposition of $Cr_7Ni-eth$. If the Raman spectrum showed the same peaks as those present in the powder spectrum of the nanomagnet given in Chapter 3 of this thesis then that would provide evidence that the molecule remained intact on the graphene surface. However, only the peaks corresponding to the graphene flake were observed in the Raman spectrum taken after the deposition. This result is

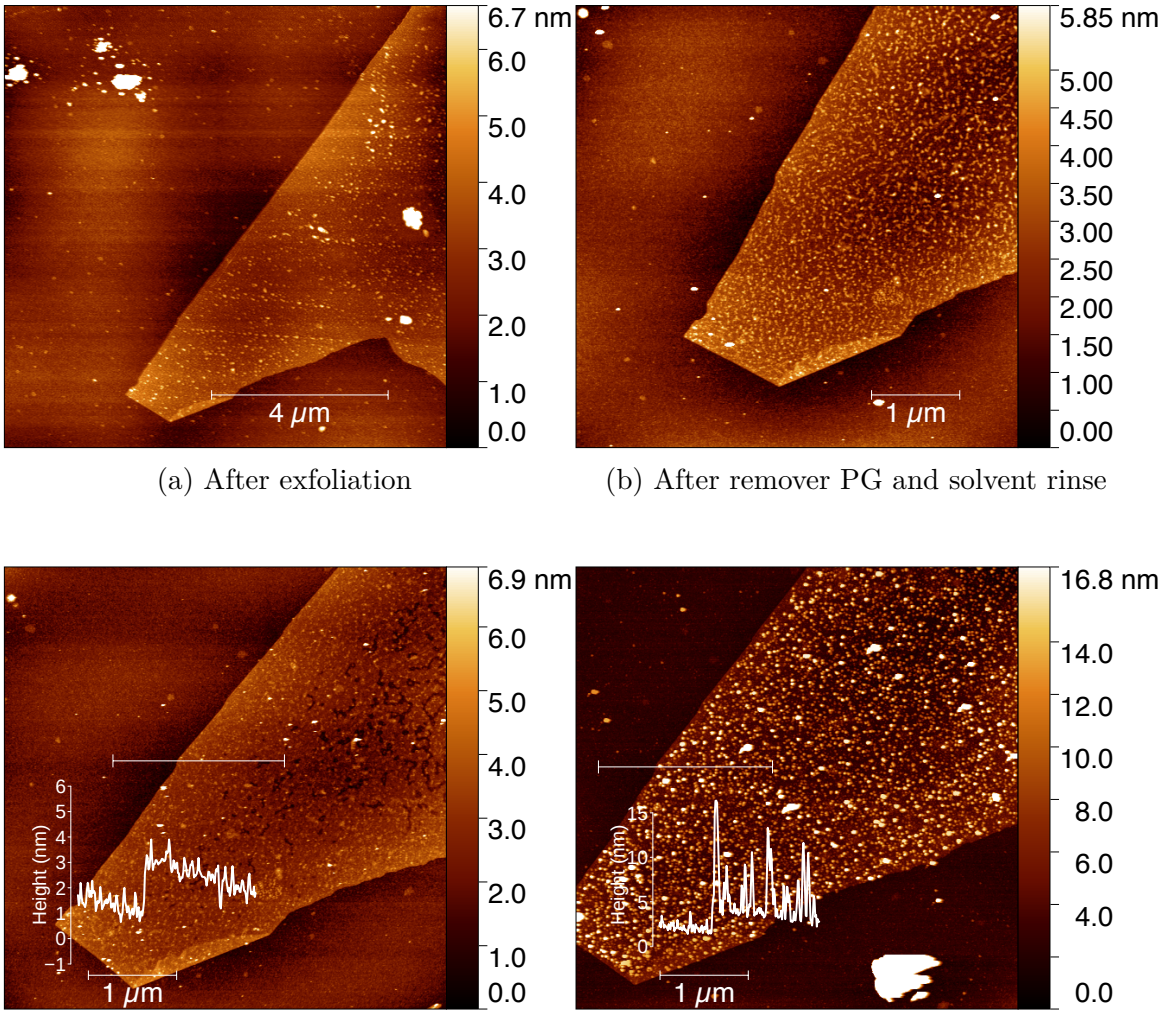

(a) After exfoliation

(b) After remover PG and solvent rinse

(c) After solvent rinse

(d) After deposition

Figure 5.11: Complete processing of a graphene flake, from exfoliation to deposition. (a) A bilayer graphene flake after exfoliation dirty with residues. (b) The same flake after being soaked in remover PG and subsequently rinsed with acetone followed by isopropanol. The surface of the flake remains contaminated and the looks more weathered. (c) The flake after a second rinse in acetone and isopropanol. Many of the residues have now been removed. (d) Deposition of Cr_7Ni-eth on the same flake. An approximately 10^{-4} M solution in chloroform was used. The flake appears decorated with molecules and is significantly rougher compared to the cleaned flake in (c).

not unexpected as due to the small number of particles on the surface, and the fact that the molecule has only a weak Raman signal, we would likely only be able to detect the nanomagnet if it experienced surface enhanced Raman scattering [11]. This phenomenon has been observed for other SMMs grafted to graphene [47], and graphene itself has been shown to be an effective substrate for surface enhanced Raman experiments [45]. However, in order to observe this property, a monolayer of the molecules would be required because otherwise the molecules not in direct contact with the surface would screen the effect.

Now that a procedure has been developed for realizing clean graphene substrates suitable to image submonolayers of molecular nanomagnets, future work will consist of performing a systematic study of depositions of all the varieties of nanomagnets described in this thesis. By analyzing the effects of the concentrations of the solutions of nanomagnets used in each deposition on the resulting surface coverage of the particles we hope to be able to quantify the propensity for each molecular species to adhere to a graphene surface. In addition to performing depositions on graphene flakes, future work will also include studies of depositions on pristine CNTs. Once samples of the nanomagnets on both graphitic surfaces are prepared then further studies can be done to determine whether the structural and magnetic properties of the molecules are retained (e.g. using STM, Raman and XPS).

Chapter 6

Summary and outlook

The field of molecular magnetism affords an exciting opportunity for the exploration of spin physics. Whether the molecular system is studied directly through traditional measurements (e.g. electron spin resonance (ESR), magnetometry) or is integrated into a spintronics device, the magnetic properties of the system exhibit a variety of quantum effects. The integration of molecular nanomagnets into nanoelectronic technologies presents a difficult engineering challenge, yet has the potential to offer significant scientific rewards. These molecular systems have been suggested as potential qubits in quantum computing, and the realization of spin-based nanoelectronics devices that have the ability to probe and manipulate the magnetic properties of a molecular nanomagnet, represents a stepping stone in the realization of these quantum information processing proposals. Much of the work presented in this thesis was toward the experimental realization of such novel spintronics devices.

As a first step, the Cr_7Ni-eth antiferromagnetic wheel was successfully synthesized, with the ultimate goal of integrating this molecular system into spin-based nanoelectronic devices. The synthetic process involved using 2-ethylhexanoic acid as the carboxylic acid in a general reaction procedure utilized for synthesizing the family of Cr_7Ni antiferromagnetic wheels. This carboxylic acid was selected in order to introduce long alkyl chains into the organic shell of the nanomagnet. It was anticipated that these long alkyl chains would interact via van der Waals forces with graphitic surfaces, forming non-covalent bonds. Consequently, the Cr_7Ni-eth variant of the Cr_7Ni family of antiferromagnetic wheels is ideal for being used in carbon-based spintronics devices. X-ray diffraction data in conjunction with electron spin resonance experiments provided evidence that supported that the synthesized molecule contained the Cr_7Ni magnetic core, while evidence for the presence of 2-ethylhexanoic acid in the organic shell of the molecule was given by Fourier transform infrared spectroscopy.

The magnetic energy spectrum of the Cr_7Ni-eth system was simulated using the isotropic coupling single-ion Hamiltonian. The ground state of the system was found to be a spin doublet. This result was expected given the antiferromagnetic coupling between the constituent metal centres in the molecule and their corresponding spins

(for Cr, $S = 3/2$, for Ni, $S = 1$). The first excited state was found to lie approximately 10 cm^{-1} (1 meV) above the ground state. Resonances were calculated at a microwave frequency of 9.4 GHz and based on the location of these resonances the ESR spectrum of the molecule was simulated. All of the widths of the peaks were set to the same value in the modeled spectrum, but the intensities of each resonance were scaled using a Boltzmann distribution. At 4 K it was found that only the resonances located in the two lowest energy states of the system would be visible in the ESR spectrum, with the resonance in the ground state being approximately ten times more intense.

Experimental continuous wave ESR (CW-ESR) data was measured for both a crystalline sample of the Cr_7Ni-eth nanomagnets and for a frozen solution of the system. The simulated ESR spectrum determined using the coupling single-ion Hamiltonian reproduced many of the features present in the data obtained for the crystalline sample at 4 K. Only two peaks were present in the experimental spectrum at $g = 1.770$ and $g = 1.945$, corresponding to the two resonances predicted by the simulation. Although the g-factors of the two peaks were not in complete agreement this is likely due to the presence of anisotropy in the system that was not taken into account in the purely isotropic Hamiltonian utilized in the simulation. Additional evidence for the presence of anisotropy was found in both measurements of the ESR spectra of multiple orientations of the crystalline sample, and in the ESR spectrum of a frozen solution of the synthesized product. As the sample tube containing the crystalline sample was rotated within the ESR cavity the location of the resonance at $g = 1.770$ shifted. Similarly, in the ESR spectra of the frozen solutions the width of the peak at $g = 1.770$ was larger compared to that in the crystalline sample. Both of these results indicate the presence of anisotropy in the system.

Much of the work described in this thesis involved characterizing the structural and magnetic properties of the syntehsized Cr_7Ni-eth species. This characterization served to confirm that the synthesis was successful and that the desired compound had been produced. Additionally, the characterization was also exploratory in nature, providing a description of the properties of the molecule. By understanding both the magnetic and structural nature of the system one can more accurately predict how the system will react when incorporated into a spintronics device. Consequently, the results obtained through these experiments will be of use in analyzing the behaviour of a realized spin-based nanoelectronics device that utilizes the Cr_7Ni-eth molecule.

One of the first steps in experimentally realizing a functioning spin-based nanoelectronics device is to determine whether a particular molecular system is a viable candidate to be incorporated into a specific device design. In order for a molecular system to be appropriate it must retain its properties when integrated into the device, without adversely affecting the properties of the nanoelectronic components. We are primarily interested in fabricating carbon-based nanoelectronics, and thus in order to determine whether the Cr_7Ni-eth species can be utilized in a carbon-based spintronics device the first step was studying how the molecule behaves when

attached to a carbon surface, namely graphene and carbon nanotubes. In order to study this behaviour a process was developed for producing and cleaning graphene flakes such that sub-monolayer concentrations of the synthesized nanomagnet could be visualized on the graphene surface. This process utilized the mechanical exfoliation technique for generating graphene flakes. The majority of the graphene flakes produced contained some form of surface contamination. This contamination was cleaned using a combination of a solvent rinse and annealing at 400° under an inert atmosphere.

A particular antiferromagnetic ring, Cr_7Ni-eth, has been synthesized and characterized, and a process for producing clean graphene flakes has been developed. Subsequent work will involve analyzing the depositions of different concentrations of Cr_7Ni-eth, as well as other molecular nanomagnets, on both graphene and pristine carbon nanotubes. Through AFM imaging, Raman spectroscopy, and other surface characterization techniques, we will study the magnetic and structural stability of each nanomagnet when deposited on the graphitic surface. From these results we can probe the nature of the interactions between different ligands present in the organic shells of the nanomagnets tested and carbon nanostructures, with the ultimate goal of fabricating a range of carbon-based molecular spintronics devices. In the event that the Cr_7Ni-eth nanomagnet does not successfully bind to graphitic surfaces then the system can be chemically modified to enhance the binding affinity of the molecule. Longer alkyl chains than those present in 2-ethylhexanoic acid, and ligands containing π-π stacking groups (e.g. aromatic rings) can be introduced into the organic shell through established methods of organic synthesis.

Additionally, future work will also include measuring the ESR spectrum of the Mn_3 family of single-molecule magnets. These molecule have been functionalized with fluorescent ligands that upon excitation with an ultraviolet light source form photo-excited triplet states. Consequently, these systems could possess interesting electron spin resonance properties through which the magnetic interactions between these triplet states and the core of the single-molecule magnets could be studied.

Molecular nanomagnets present an exciting opportunity for the exploration of spin physics. The fabrication of nanoelectronic devices that incorporate molecular nanomagnets is a difficult engineering challenge, but one that affords the opportunity to both probe and manipulate the properties of these systems. The research presented in this thesis describes the first steps towards realizing such devices.

References

[1] M. Affronte, I. Casson, M. Evangelisti, A. Candini, S. Carretta, C. A. Muryn, S. J. Teat, G. A. Timco, W. Wernsdorfer, and R. E. P. Winpenny. "Linking rings through diamines and clusters: Exploring synthetic methods for making magnetic quantum gates". In: *Angewandte Chemie International Edition* 44.40 (2005), pp. 6496–6500.

[2] D. I. Alexandropoulos, A. M. Mowson, M. Pilkington, V. Bekiari, G. Christou, and T. C. Stamatatos. "Emissive molecular nanomagnets: introducing optical properties in triangular oximato {Mn III 3} SMMs from the deliberate replacement of simple carboxylate ligands with their fluorescent analogues". In: *Dalton Transactions* 43.5 (2014), pp. 1965–1969.

[3] A. Ardavan, O. Rival, J. J. Morton, S. J. Blundell, A. M. Tyryshkin, G. A. Timco, and R. E. Winpenny. "Will spin-relaxation times in molecular magnets permit quantum information processing?" In: *Physical Review Letters* 98.5 (2007), p. 057201.

[4] B. Ballesteros, T. B. Faust, C.-F. Lee, D. A. Leigh, C. A. Muryn, R. G. Pritchard, D. Schultz, S. J. Teat, G. A. Timco, and R. E. P. Winpenny. "Synthesis, Structure, and Dynamic Properties of Hybrid Organic- Inorganic Rotaxanes". In: *Journal of the American Chemical Society* 132.43 (2010), pp. 15435–15444.

[5] V. Balzani, A. Credi, and M. Venturi. "The Bottom-Up Approach to Molecular-Level Devices and Machines". In: *Chemistry-A European Journal* 8.24 (2002), pp. 5524–5532.

[6] A. L. Barra, D. Gatteschi, and R. Sessoli. "High-frequency EPR spectra of a molecular nanomagnet: Understanding quantum tunneling of the magnetization". In: *Physical Review B* 56.13 (1997), p. 8192.

[7] A.-L. Barra, A. Caneschi, A. Cornia, D. Gatteschi, L. Gorini, L.-P. Heiniger, R. Sessoli, and L. Sorace. "The origin of transverse anisotropy in axially symmetric single molecule magnets". In: *Journal of the American Chemical Society* 129.35 (2007), pp. 10754–10762.

[8] L. Bogani and W. Wernsdorfer. "A perspective on combining molecular nanomagnets and carbon nanotube electronics". In: *Inorganica Chimica Acta* 361.14 (2008), pp. 3807–3819.

[9] L. Bogani and W. Wernsdorfer. “Molecular spintronics using single-molecule magnets”. In: *Nature Materials* 7.3 (2008), pp. 179–186.

[10] R. Caciuffo, T. Guidi, G. Amoretti, S. Carretta, E. Liviotti, P. Santini, C. Mondelli, G. Timco, C. Muryn, and R. Winpenny. “Spin dynamics of heterometallic Cr 7 M wheels (M= Mn, Zn, Ni) probed by inelastic neutron scattering”. In: *Physical Review B* 71.17 (2005), p. 174407.

[11] A. Campion and P. Kambhampati. “Surface-enhanced Raman scattering”. In: *Chem. Soc. Rev.* 27.4 (1998), pp. 241–250.

[12] A. Caneschi, D. Gatteschi, R. Sessoli, A. L. Barra, L. C. Brunel, and M. Guillot. “Alternating current susceptibility, high field magnetization, and millimeter band EPR evidence for a ground S= 10 state in [Mn12O12 (Ch3COO) 16 (H2O) 4]. 2CH3COOH. 4H2O”. In: *Journal of the American Chemical Society* 113.15 (1991), pp. 5873–5874.

[13] S. Carretta, J. Van Slageren, T. Guidi, E. Liviotti, C. Mondelli, D. Rovai, A. Cornia, A. Dearden, F. Carsughi, M. Affronte, C. D. Frost, R. E. P. Winpenny, D. Gatteschi, G. Amoretti, and R. Caciuffo. “Microscopic spin Hamiltonian of a Cr 8 antiferromagnetic ring from inelastic neutron scattering”. In: *Physical Review B* 67.9 (2003), p. 094405.

[14] N. E. Chakov, M. Soler, W. Wernsdorfer, K. A. Abboud, and G. Christou. “Single-molecule magnets: Structural characterization, magnetic properties, and 19F NMR spectroscopy of a Mn12 family spanning three oxidation levels”. In: *Inorganic Chemistry* 44.15 (2005), pp. 5304–5321.

[15] A. R. Champagne, A. N. Pasupathy, and D. C. Ralph. “Mechanically adjustable and electrically gated single-molecule transistors”. In: *Nano letters* 5.2 (2005), pp. 305–308.

[16] J. I. Cirac and P. Zoller. “Quantum computations with cold trapped ions”. In: *Physical review letters* 74.20 (1995), p. 4091.

[17] J. Clarke and F. K. Wilhelm. “Superconducting quantum bits”. In: *Nature* 453.7198 (2008), pp. 1031–1042.

[18] J.-P. Cleuziou, W. Wernsdorfer, V. Bouchiat, T. Ondarçuhu, and M. Monthioux. “Carbon nanotube superconducting quantum interference device”. In: *Nature Nanotechnology* 1.1 (2006), pp. 53–59.

[19] A. Cornia, R. Sessoli, L. Sorace, D. Gatteschi, A. Barra, and C. Daiguebonne. “Origin of Second-Order Transverse Magnetic Anisotropy in M n 12-Acetate”. In: *Physical review letters* 89.25 (2002), p. 257201.

[20] A. De Cian, M. Moussavi, J. Fischer, and R. Weiss. “Synthesis, structure, and spectroscopic and magnetic properties of lutetium (III) phthalocyanine derivatives: LuPc2. CH2Cl2 and [LuPc (OAc)(H2O) 2]. H2O. 2CH3OH”. In: *Inorganic Chemistry* 24.20 (1985), pp. 3162–3167.

[21] A. Ferrari, J. Meyer, V. Scardaci, C. Casiraghi, M. Lazzeri, F. Mauri, S. Piscanec, D. Jiang, K. Novoselov, S. Roth, and A. K. Geim. "Raman spectrum of graphene and graphene layers". In: *Physical review letters* 97.18 (2006), p. 187401.

[22] J. R. Friedman, M. Sarachik, J. Tejada, and R. Ziolo. "Macroscopic measurement of resonant magnetization tunneling in high-spin molecules". In: *Physical Review Letters* 76.20 (1996), p. 3830.

[23] J. R. Friedman and M. P. Sarachik. "Single-molecule nanomagnets". In: *arXiv preprint arXiv:1001.4194* (2010).

[24] M. Ganzhorn, S. Klyatskaya, M. Ruben, and W. Wernsdorfer. "Carbon Nanotube Nanoelectromechanical Systems as Magnetometers for Single-Molecule Magnets". In: *ACS Nano* 7.7 (2013), pp. 6225–6236.

[25] M. Ganzhorn, S. Klyatskaya, M. Ruben, and W. Wernsdorfer. "Strong spin-phonon coupling between a single-molecule magnet and a carbon nanotube nanoelectromechanical system". In: *Nature Nanotechnology* 8.3 (2013), pp. 165–169.

[26] M. Ganzhorn and W. Wernsdorfer. "Molecular Quantum Spintronics Using Single-Molecule Magnets". In: *Molecular Magnets*. Springer, 2014, pp. 319–364.

[27] X. Gao and X. S. Tang. "Effective reduction of graphene oxide thin films by a fluorinating agent: Diethylaminosulfur trifluoride". In: *Carbon* 76 (2014), pp. 133–140.

[28] D. Gatteschi, R. Sessoli, and J. Villain. *Molecular nanomagnets*. Oxford University Press, 2006.

[29] N. A. Gershenfeld and I. L. Chuang. "Bulk spin-resonance quantum computation". In: *science* 275.5298 (1997), pp. 350–356.

[30] A. Ghirri, V. Corradini, C. Cervetti, A. Candini, U. Del Pennino, G. Timco, R. J. Pritchard, C. A. Muryn, R. E. Winpenny, and M. Affronte. "Deposition of Functionalized Cr7Ni Molecular Rings on Graphite from the Liquid Phase". In: *Advanced Functional Materials* 20.10 (2010), pp. 1552–1560.

[31] L. K. Grover. "Quantum mechanics helps in searching for a needle in a haystack". In: *Physical review letters* 79.2 (1997), p. 325.

[32] M. D. Hanwell, D. E. Curtis, D. C. Lonie, T. Vandermeersch, E. Zurek, and G. R. Hutchison. "Avogadro: An advanced semantic chemical editor, visualization, and analysis platform." In: *J. Cheminformatics* 4.1 (2012), p. 17.

[33] H. Heersche, Z. De Groot, J. Folk, H. Van Der Zant, C. Romeike, M. Wegewijs, L. Zobbi, D. Barreca, E. Tondello, and A. Cornia. "Electron transport through single Mn 12 molecular magnets". In: *Physical Review Letters* 96.20 (2006), p. 206801.

[34] W. S. Hummers Jr and R. E. Offeman. "Preparation of graphitic oxide". In: *Journal of the American Chemical Society* 80.6 (1958), pp. 1339–1339.

[35] M.-H. Jo, J. E. Grose, K. Baheti, M. M. Deshmukh, J. J. Sokol, E. M. Rumberger, D. N. Hendrickson, J. R. Long, H. Park, and D. Ralph. "Signatures of molecular magnetism in single-molecule transport spectroscopy". In: *Nano Letters* 6.9 (2006), pp. 2014–2020.

[36] E. Knill, R. Laflamme, and G. J. Milburn. "A scheme for efficient quantum computation with linear optics". In: *nature* 409.6816 (2001), pp. 46–52.

[37] F. K. Larsen, E. J. McInnes, H. E. Mkami, J. Overgaard, S. Piligkos, G. Rajaraman, E. Rentschler, A. A. Smith, G. M. Smith, V. Boote, M. Jennings, G. A. Timco, and R. E. P. Winpenny. "Synthesis and characterization of heterometallic Cr_7M wheels". In: *Angewandte Chemie International Edition* 42.1 (2003), pp. 101–105.

[38] F. K. Larsen, J. Overgaard, S. Parsons, E. Rentschler, A. A. Smith, G. A. Timco, and R. E. Winpenny. "Horseshoes, Rings, and Distorted Rings: Studies of Cyclic Chromium-Fluoride Cages". In: *Angewandte Chemie* 115.48 (2003), pp. 6160–6163.

[39] B. Lassagne, D. Ugnati, and M. Respaud. "Ultrasensitive magnetometers based on carbon-nanotube mechanical resonators". In: *Physical Review Letters* 107.13 (2011), p. 130801.

[40] C. Lau, J. Mol, J. Warner, and G. Briggs. "Nanoscale control of graphene electrodes". In: *Physical Chemistry Chemical Physics* 16.38 (2014), pp. 20398–20401.

[41] R. H. Laye, F. K. Larsen, J. Overgaard, C. A. Muryn, E. J. McInnes, E. Rentschler, V. Sanchez, S. J. Teat, H. U. Güdel, O. Waldmann, G. A. Timco, and R. E. P. Winpenny. "A family of heterometallic wheels containing potentially fourteen hundred siblings". In: *Chemical Communications* 9 (2005), pp. 1125–1127.

[42] R. B. Lehoucq, D. C. Sorensen, and C. Yang. *ARPACK users' guide: solution of large-scale eigenvalue problems with implicitly restarted Arnoldi methods*. Vol. 6. Siam, 1998.

[43] M. N. Leuenberger and D. Loss. "Quantum computing in molecular magnets". In: *Nature* 410.6830 (2001), pp. 789–793.

[44] S. M. Lindsay and M. A. Ratner. "Molecular transport junctions: Clearing mists". In: *Advanced Materials* 19.1 (2007), pp. 23–31.

[45] X. Ling, L. Xie, Y. Fang, H. Xu, H. Zhang, J. Kong, M. S. Dresselhaus, J. Zhang, and Z. Liu. "Can graphene be used as a substrate for Raman enhancement?" In: *Nano letters* 10.2 (2009), pp. 553–561.

[46] T. Lis. “Preparation, structure, and magnetic properties of a dodecanuclear mixed-valence manganese carboxylate”. In: *Acta Crystallographica Section B: Structural Crystallography and Crystal Chemistry* 36.9 (1980), pp. 2042–2046.

[47] M. Lopes, A. Candini, M. Urdampilleta, A. Reserbat-Plantey, V. Bellini, S. Klyatskaya, L. Marty, M. Ruben, M. Affronte, W. Wernsdorfer, and N. Bendiab. “Surface-enhanced Raman signal for terbium single-molecule magnets grafted on graphene”. In: *ACS nano* 4.12 (2010), pp. 7531–7537.

[48] D. Loss and D. P. DiVincenzo. “Quantum computation with quantum dots”. In: *Physical Review A* 57.1 (1998), p. 120.

[49] M. Mannini, P. Sainctavit, R. Sessoli, C. Cartier dit Moulin, F. Pineider, M.-A. Arrio, A. Cornia, and D. Gatteschi. “XAS and XMCD Investigation of Mn12 Monolayers on Gold”. In: *Chemistry-A European Journal* 14.25 (2008), pp. 7530–7535.

[50] F. Meier, J. Levy, and D. Loss. “Quantum computing with spin cluster qubits”. In: *Physical review letters* 90.4 (2003), p. 047901.

[51] F. Meier and D. Loss. “Thermodynamics and spin-tunneling dynamics in ferric wheels with excess spin”. In: *Physical Review B* 64.22 (2001), p. 224411.

[52] D. A. Muller, T. Sorsch, S. Moccio, F. Baumann, K. Evans-Lutterodt, and G. Timp. “The electronic structure at the atomic scale of ultrathin gate oxides”. In: *Nature* 399.6738 (1999), pp. 758–761.

[53] D. Nečas and P. Klapetek. “Gwyddion: an open-source software for SPM data analysis”. In: *Open Physics* 10.1 (2012), pp. 181–188.

[54] M. A. Nielsen and I. L. Chuang. *Quantum computation and quantum information*. Cambridge university press, 2010.

[55] J. North, R. Achey, and N. Dalal. “Low-frequency Raman modes of the single-molecule magnets Mn 12-acetate and Fe 8 Br 8 and their analogs”. In: *Physical Review B* 66.17 (2002), p. 174437.

[56] K. Novoselov, D. Jiang, F. Schedin, T. Booth, V. Khotkevich, S. Morozov, and A. Geim. “Two-dimensional atomic crystals”. In: *Proceedings of the National Academy of Sciences of the United States of America* 102.30 (2005), pp. 10451–10453.

[57] J. Park, A. N. Pasupathy, J. I. Goldsmith, C. Chang, Y. Yaish, J. R. Petta, M. Rinkoski, J. P. Sethna, H. D. Abruña, P. L. McEuen, and D. C. Ralph. “Coulomb blockade and the Kondo effect in single-atom transistors”. In: *Nature* 417.6890 (2002), pp. 722–725.

[58] M. L. Perrin, E. Burzur, and H. S. van der Zant. “Single-molecule transistors”. In: *Chemical Society Reviews* 44.4 (2015), pp. 902–919.

[59] S. Piligkos, H. Weihe, E. Bill, F. Neese, H. El Mkami, G. M. Smith, D. Collison, G. Rajaraman, G. A. Timco, R. E. Winpenny, and E. J. L. McInnes. "EPR Spectroscopy of a Family of $Cr_7^{III}M^{II}$ (M=Cd, Zn, Mn, Ni) Wheels: Studies of Isostructural Compounds with Different Spin Ground States". In: *Chemistry-A European Journal* 15.13 (2009), pp. 3152–3167.

[60] F. Pineider, M. Mannini, C. Danieli, L. Armelao, F. M. Piras, A. Magnani, A. Cornia, and R. Sessoli. "Deposition of intact tetrairon (III) single molecule magnet monolayers on gold: an STM, XPS, and ToF-SIMS investigation". In: *Journal of Materials Chemistry* 20.1 (2010), pp. 187–194.

[61] R. Sessoli, D. Gatteschi, A. Caneschi, and M. Novak. "Magnetic bistability in a metal-ion cluster". In: *Nature* 365.6442 (1993), pp. 141–143.

[62] P. W. Shor. "Polynomial-time algorithms for prime factorization and discrete logarithms on a quantum computer". In: *SIAM journal on computing* 26.5 (1997), pp. 1484–1509.

[63] H. Song, Y. Kim, Y. H. Jang, H. Jeong, M. A. Reed, and T. Lee. "Observation of molecular orbital gating". In: *Nature* 462.7276 (2009), pp. 1039–1043.

[64] H. Song, Y. Kim, H. Jeong, M. A. Reed, and T. Lee. "Coherent Tunneling Transport in Molecular Junctions†". In: *The Journal of Physical Chemistry C* 114.48 (2010), pp. 20431–20435.

[65] T. C. Stamatatos, D. Foguet-Albiol, C. C. Stoumpos, C. P. Raptopoulou, A. Terzis, W. Wernsdorfer, S. P. Perlepes, and G. Christou. "Initial example of a triangular single-molecule magnet from ligand-induced structural distortion of a $[Mn_3^{III}O]^{7+}$ complex". In: *Journal of the American Chemical Society* 127.44 (2005), pp. 15380–15381.

[66] D. Strachan, D. Smith, D. Johnston, T.-H. Park, M. J. Therien, D. Bonnell, and A. Johnson. "Controlled fabrication of nanogaps in ambient environment for molecular electronics". In: *Applied Physics Letters* 86.4 (2005), p. 043109.

[67] K. L. Taft, C. D. Delfs, G. C. Papaefthymiou, S. Foner, D. Gatteschi, and S. J. Lippard. "$[Fe(OMe)_2(O_2CCH_2Cl)]_{10}$, a Molecular Ferric Wheel". In: *Journal of the American Chemical Society* 116.3 (1994), pp. 823–832.

[68] J. Tejada, E. Chudnovsky, E. Del Barco, J. Hernandez, and T. Spiller. "Magnetic qubits as hardware for quantum computers". In: *Nanotechnology* 12.2 (2001), p. 181.

[69] S. Thiele, F. Balestro, R. Ballou, S. Klyatskaya, M. Ruben, and W. Wernsdorfer. "Electrically driven nuclear spin resonance in single-molecule magnets". In: *Science* 344.6188 (2014), pp. 1135–1138.

[70] G. A. Timco, A. S. Batsanov, F. K. Larsen, C. A. Muryn, J. Overgaard, S. J. Teat, and R. E. Winpenny. "Influencing the nuclearity and constitution of heterometallic rings via templates". In: *Chemical Communications* 29 (2005), pp. 3649–3651.

[71] G. A. Timco, S. Carretta, F. Troiani, F. Tuna, R. J. Pritchard, C. A. Muryn, E. J. McInnes, A. Ghirri, A. Candini, P. Santini, G. Amoretti, M. Affronte, and R. E. P. Winpenny. "Engineering the coupling between molecular spin qubits by coordination chemistry". In: *Nature Nanotechnology* 4.3 (2009), pp. 173–178.

[72] G. A. Timco, T. B. Faust, F. Tuna, and R. E. Winpenny. "Linking heterometallic rings for quantum information processing and amusement". In: *Chemical Society Reviews* 40.6 (2011), pp. 3067–3075.

[73] G. A. Timco, E. J. McInnes, R. G. Pritchard, F. Tuna, and R. E. Winpenny. "Heterometallic rings made from chromium stick together easily". In: *Angewandte Chemie* 120.50 (2008), pp. 9827–9830.

[74] F. Troiani, M. Affronte, S. Carretta, P. Santini, and G. Amoretti. "Proposal for quantum gates in permanently coupled antiferromagnetic spin rings without need of local fields". In: *Physical review letters* 94.19 (2005), p. 190501.

[75] F. Troiani, A. Ghirri, M. Affronte, S. Carretta, P. Santini, G. Amoretti, S. Piligkos, G. Timco, and R. Winpenny. "Molecular engineering of antiferromagnetic rings for quantum computation". In: *Physical Review Letters* 94.20 (2005), p. 207208.

[76] M. Urdampilleta, S. Klyatskaya, J.-P. Cleuziou, M. Ruben, and W. Wernsdorfer. "Supramolecular spin valves". In: *Nature Materials* 10.7 (2011), pp. 502–506.

[77] R. Vincent, S. Klyatskaya, M. Ruben, W. Wernsdorfer, and F. Balestro. "Electronic read-out of a single nuclear spin using a molecular spin transistor". In: *Nature* 488.7411 (2012), pp. 357–360.

[78] L. Vitali, S. Fabris, A. M. Conte, S. Brink, M. Ruben, S. Baroni, and K. Kern. "Electronic structure of surface-supported bis (phthalocyaninato) terbium (III) single molecular magnets". In: *Nano letters* 8.10 (2008), pp. 3364–3368.

[79] O. Waldmann, C. Dobe, H. Mutka, A. Furrer, and H. Güdel. "Neel-vector tunneling in antiferromagnetic molecular clusters". In: *Physical review letters* 95.5 (2005), p. 057202.

[80] O. Waldmann, T. C. Stamatatos, G. Christou, H. Güdel, I. Sheikin, and H. Mutka. "Quantum phase interference and Néel-vector tunneling in antiferromagnetic molecular wheels". In: *Physical review letters* 102.15 (2009), p. 157202.

[81] C. Wedge, G. Timco, E. Spielberg, R. George, F. Tuna, S. Rigby, E. McInnes, R. Winpenny, S. Blundell, and A. Ardavan. "Chemical engineering of molecular qubits". In: *Physical Review Letters* 108.10 (2012), p. 107204.

[82] G. F. Whitehead, B. Cross, L. Carthy, V. A. Milway, H. Rath, A. Fernandez, S. L. Heath, C. A. Muryn, R. G. Pritchard, S. J. Teat, G. A. Timco, and R. E. P. Winpenny. "Rings and threads as linkers in metal–organic frameworks and poly-rotaxanes". In: *Chemical Communications* 49.65 (2013), pp. 7195–7197.

[83] G. F. Whitehead, J. Ferrando-Soria, L. G. Christie, N. F. Chilton, G. A. Timco, F. Moro, and R. E. Winpenny. "The acid test: the chemistry of carboxylic acid functionalised {Cr 7 Ni} rings". In: *Chemical Science* 5.1 (2014), pp. 235–239.

[84] K. Willick. "Towards magnetic force sensing of single molecules using suspended carbon nanotubes". In: *MSc Thesis, University of Waterloo* (2014).

[85] K. Willick, C. Haapamaki, and J. Baugh. "Sensitive magnetic force detection with a carbon nanotube resonator". In: *Journal of Applied Physics* 115.11 (2014), p. 114501.

[86] A. Wilson, J. Lawrence, E. Yang, M. Nakano, D. Hendrickson, and S. Hill. "Magnetization tunneling in high-symmetry single-molecule magnets: Limitations of the giant spin approximation". In: *Physical Review B* 74.14 (2006), p. 140403.

Appendices

Appendix A

Additional vibrational spectra

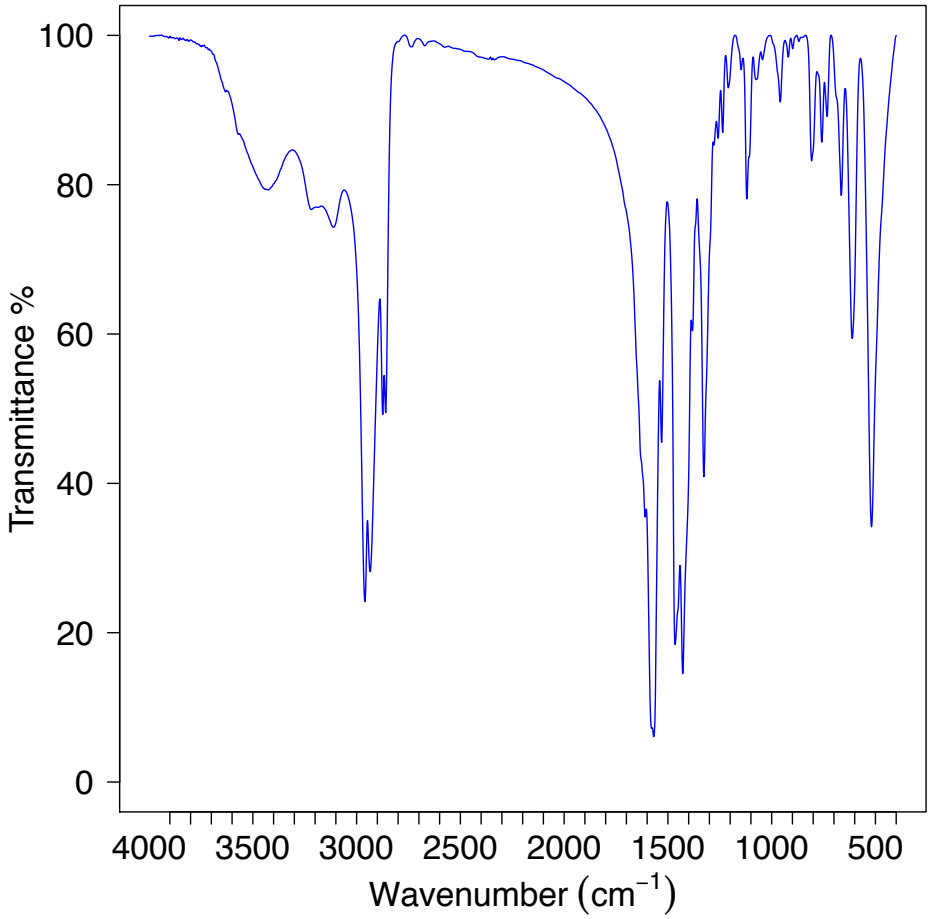

Figure A.1: The FTIR spectrum of a KBr pellet of Cr_7Ni-eth.

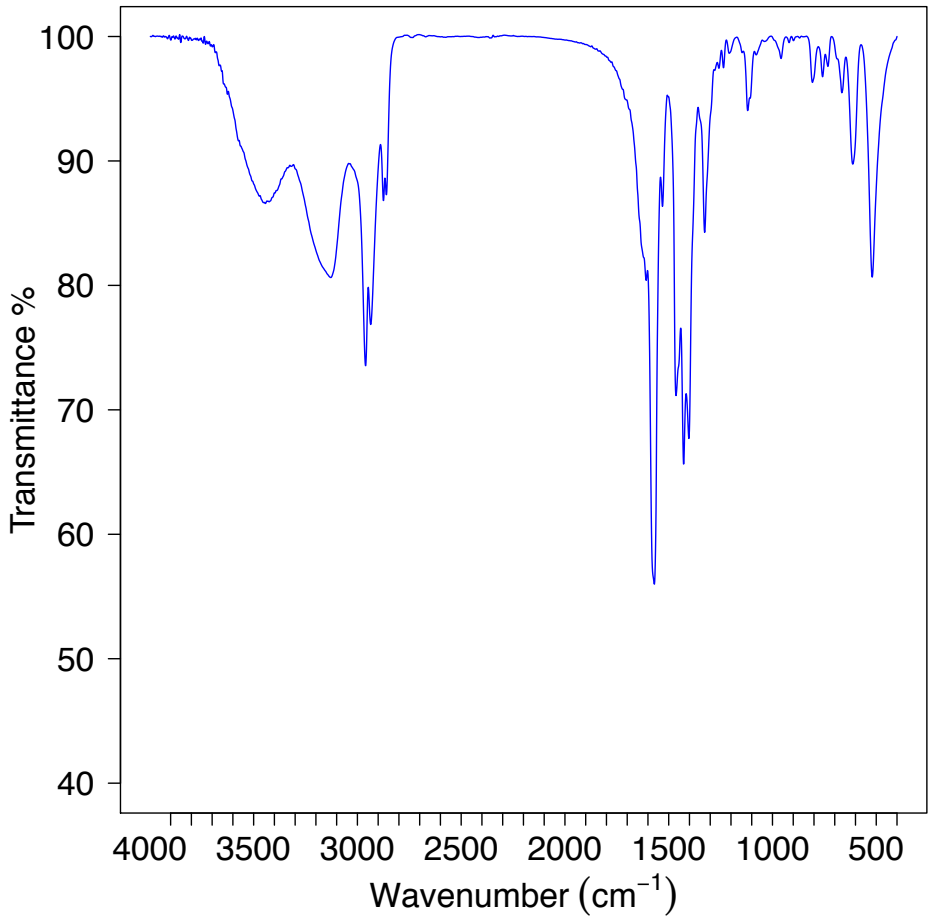

Figure A.2: The FTIR spectrum of a KBr pellet of Cr_7Ni-eth (dipropylamine).

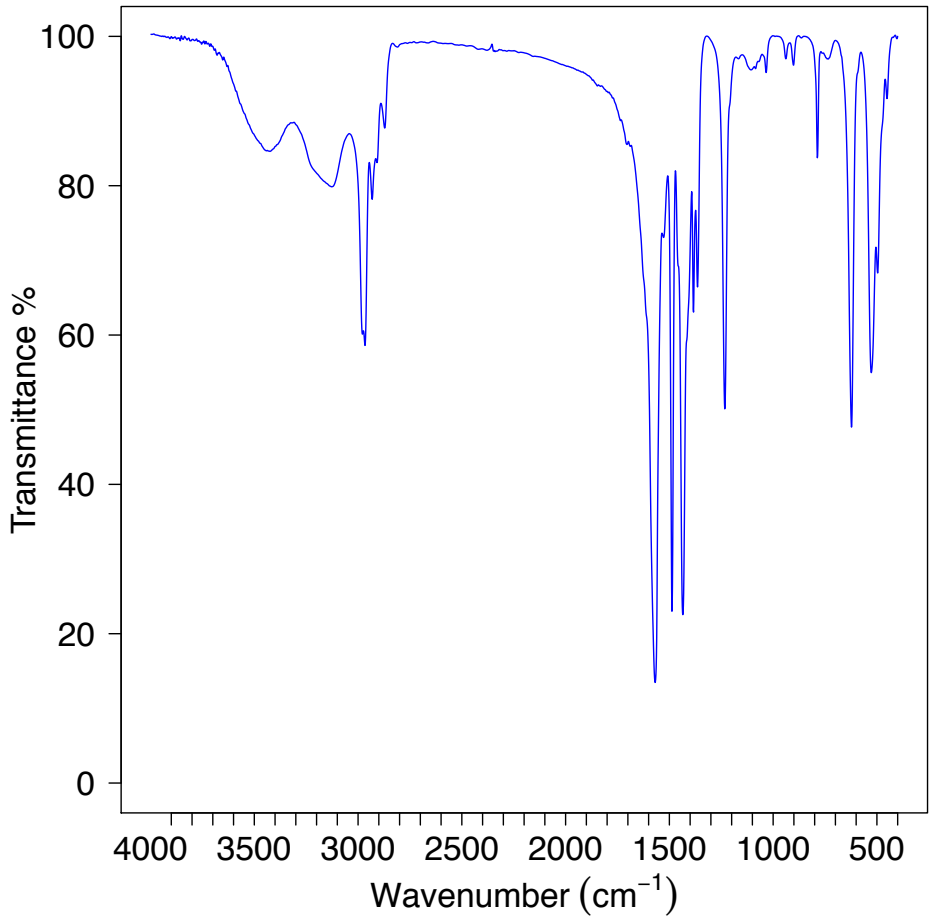

Figure A.3: The FTIR spectrum of a KBr pellet of a previously synthesized sample of the antiferromagnetic wheel Cr_7Mn. The carboxylic acid used in the synthesis was pivalic acid and the secondary amine was diethylamine.

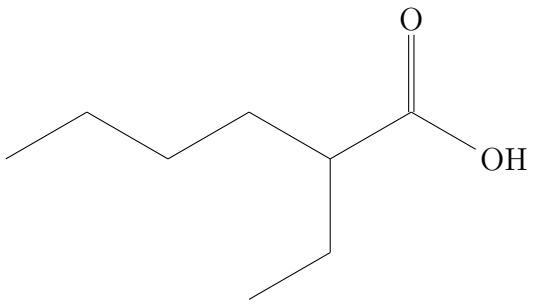

(a)

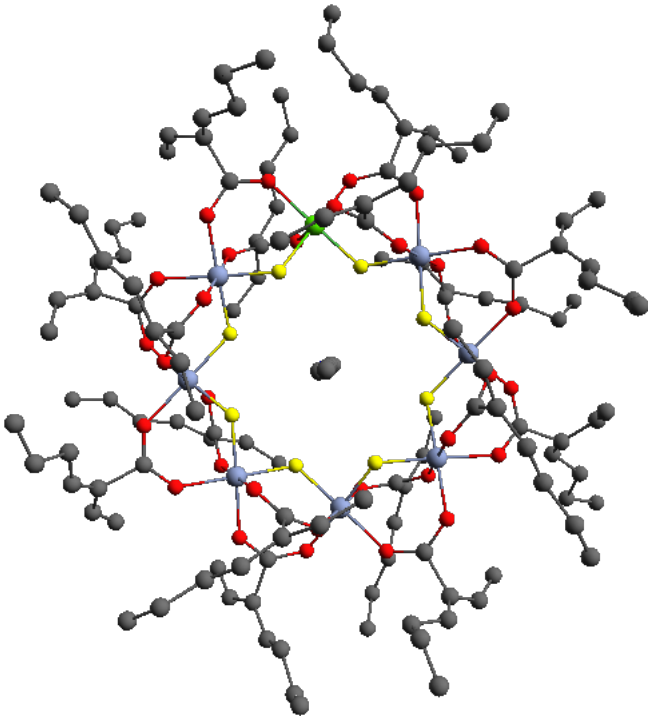

(b)

Figure A.4: The chemical structure of (a) 2-ethylhexanoic acid and (b) $Cr_7Ni{-}eth$; in the above structure di-n-propylamine was the amine used in the reaction [30]. Atom colours: Cr/Ni green; F yellow; O red; C black; N cyan.

Cr_7Ni-eth	Cr_7Ni-eth (p)	Cr_7Mn
Wavenumber (cm^{-1})	Wavenumber (cm^{-1})	Wavenumber (cm^{-1})
3425.49	3443.40	3424.42
3110.98	3128.00	3127.29
2959.99	2960.57	2966.46
2934.83	2935.74	2932.01
2874.06	2874.45	2871.49
2859.82	2860.26	1568.45
1567.92	1569.10	1487.17
1530.34	1529.89	1435.13
1465.37	1464.82	1383.97
1428.32	1427.95	1364.34
1381.72	1402.69	1232.71
1326.46	1326.67	1107.09
1235.96	1235.91	1033.59
1208.96	1208.44	938.73
1119.81	1119.35	901.81
958.71	958.62	786.53
807.49	807.44	622.18
758.41	758.50	
732.84	732.80	
664.53	665.73	
611.85	612.94	
518.74	519.48	

Table A.1: Selected peaks from the FTIR spectra of the two synthesized derivatives of the Cr_7Ni family, and from the spectrum of a previously synthesized sample of the Cr_7Mn wheel.

A basic analysis of the collected FTIR data for the heterometallic Cr_7M antiferromagnetic wheels yields the following observations:

- The FTIR spectra of the Cr_7Ni-eth wheel and the Cr_7Ni-eth (p) wheel are very similar. Considering, these systems only differ in the amine used in the reaction, this result is expected.
- All three spectra contain peaks at approximately 2900 cm^{-1} and 1575 cm^{-1} corresponding to alkyl C-H stretching and C-O stretching due to the presence of a carboxylate ion. The cluster of peaks around 2900 cm^{-1} in the Cr_7Ni derivatives have the same form compared to that in the Cr_7Mn spectrum indicating that these peaks are likely due to the C-H stretching in the carboxylate ion ligands.
- The similarities in the fingerprint region of the spectra of the Cr_7Ni derivatives indicate the large degree to which the two systems are alike. The fingerprint

region is the set of peaks between 500 cm^{-1} and 1500 cm^{-1} that are due to the multitude of bending vibrations in the molecule.

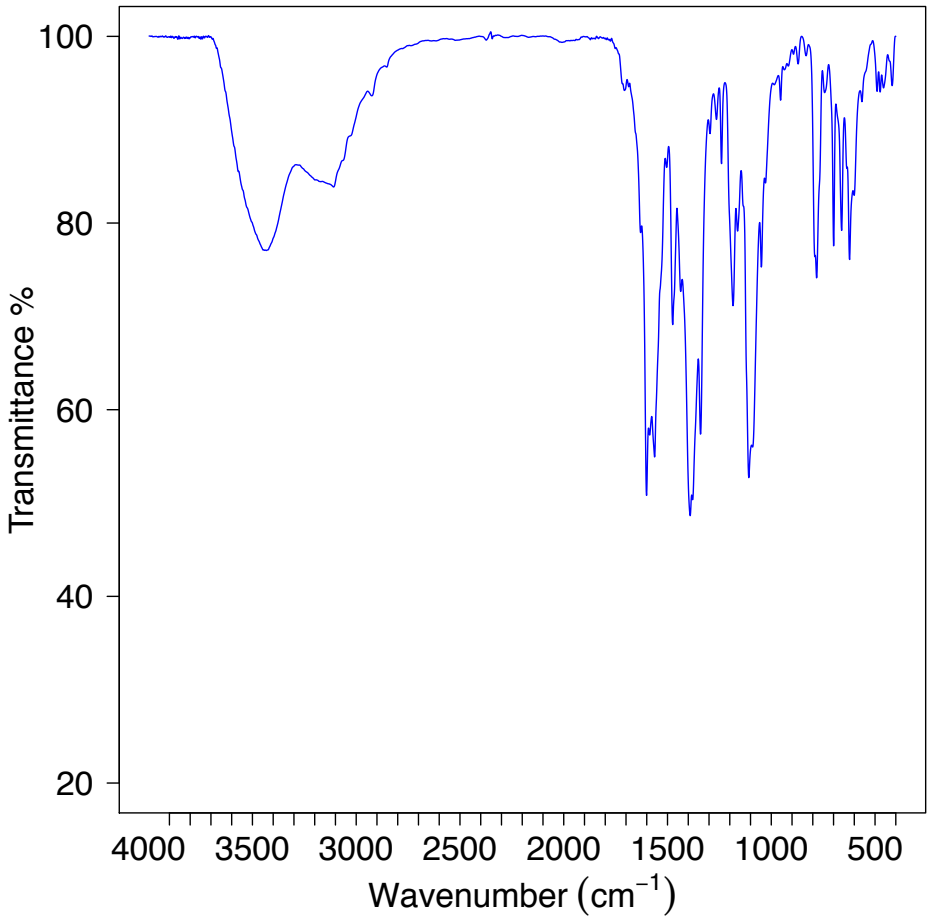

Figure A.5: The FTIR spectrum of a KBr pellet of Mn_3-naph.

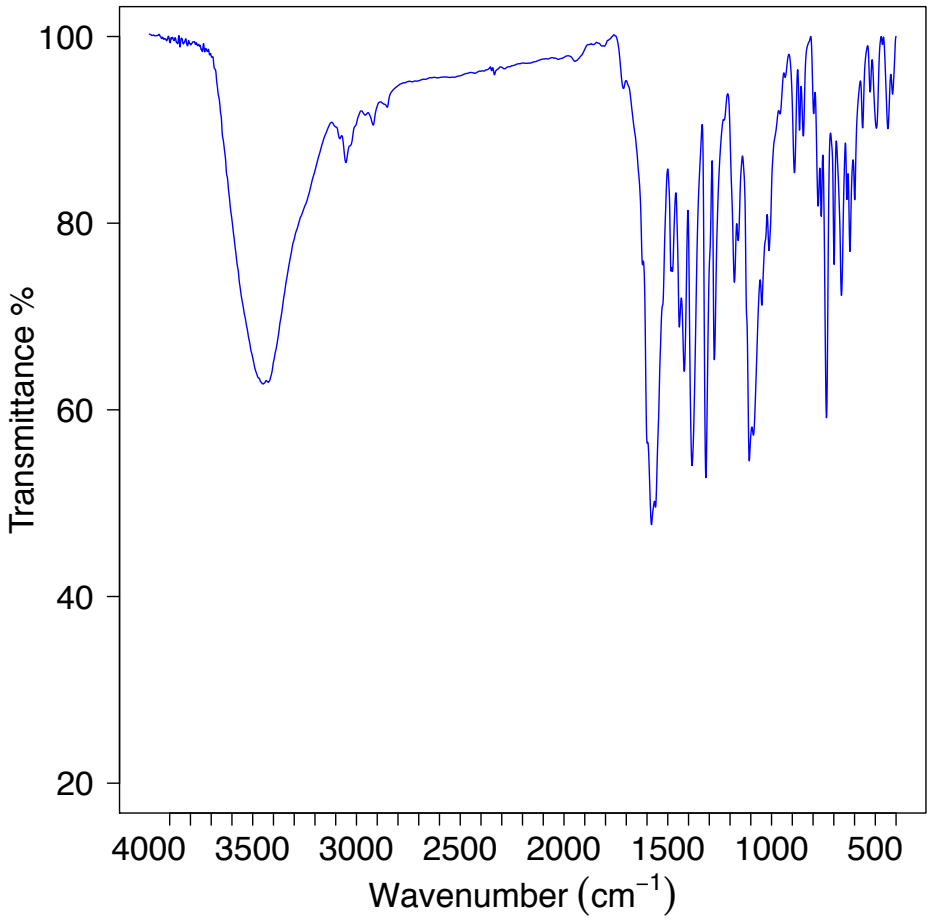

Figure A.6: The FTIR spectrum of a KBr pellet of Mn_3-anth.

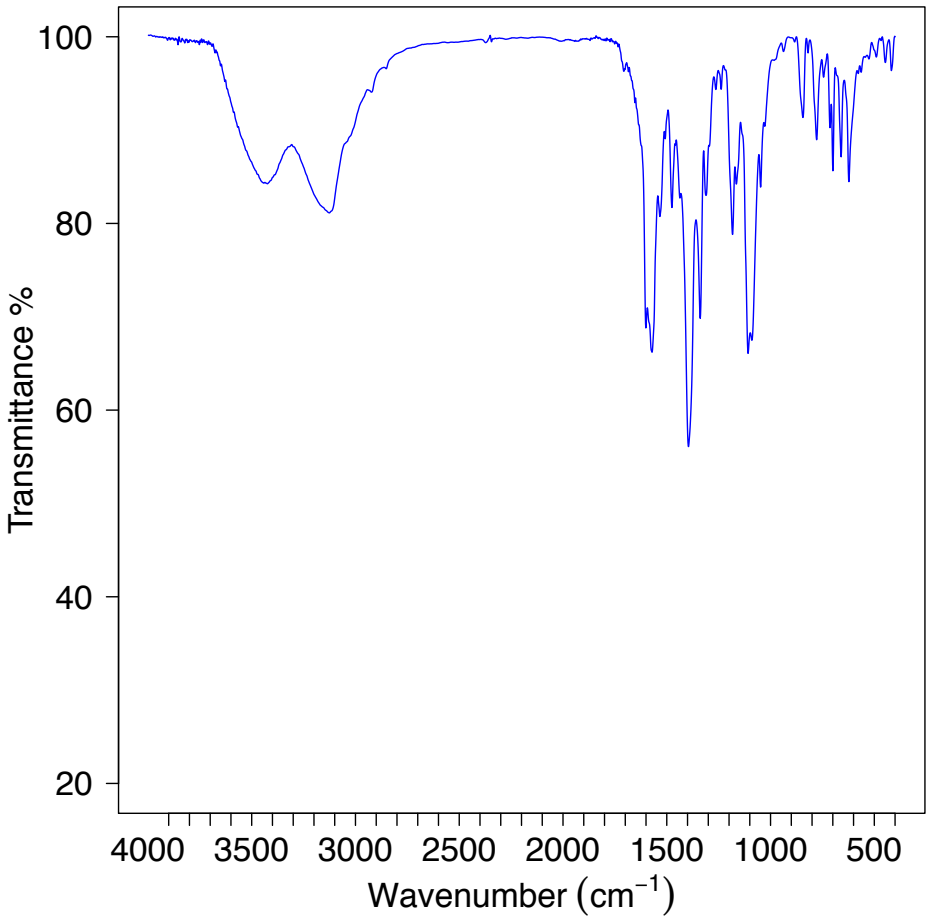

Figure A.7: The FTIR spectrum of a KBr pellet of Mn_3-pyr.

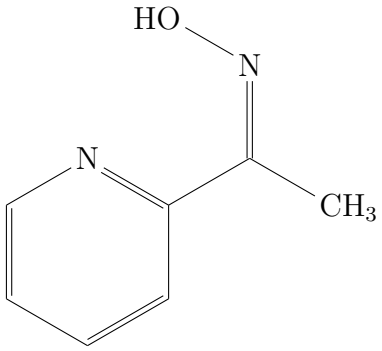

(a)

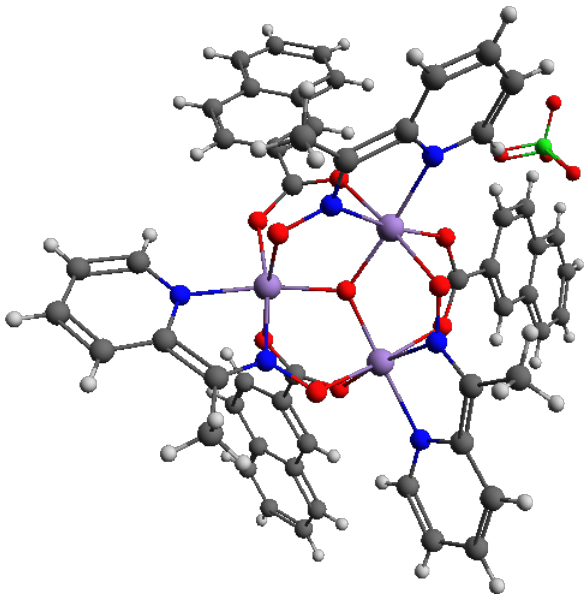

Figure A.8: The structure of the chelating ligand methyl 2-pyridyl ketone oxime and of the Mn_3−naph SMM [2]. Atom colours: Mn, purple, O, red; N, blue; C, grey; Cl, green; H, white.

Mn_3-naph	Mn_3-anth	Mn_3-pyr
Wavenumber (cm^{-1})	Wavenumber (cm^{-1})	Wavenumber (cm^{-1})
3432.86	3450.19	3424.26
3108.80	3050.87	3125.89
1601.00	1578.35	1600.66
1561.91	1477.20	1570.75
1475.02	1420.44	1475.06
1390.66	1383.16	1395.42
1340.62	1316.32	1338.70
1239.80	1275.53	1310.58
1184.03	1178.87	1183.02
1162.27	1160.78	1164.62
1108.25	1107.21	1108.12
1047.48	1046.86	1047.70
954.91	1012.01	843.73
781.32	889.42	777.76
742.91	775.36	744.32
699.40	735.10	713.28
660.99	698.48	699.41
622.83	663.06	659.92
562.93	622.22	622.54
	561.04	563.27

Table A.2: Selected peaks from the FTIR spectra of the Mn_3 family of SMMs.

A basic analysis of the collected FTIR data for the family of Mn_3 SMMs yields the following observations:

- All three spectra contain the same cluster of peaks between approximately 1045 cm^{-1} and 1185 cm^{-1}. Therefore, these peaks likely correspond to the vibrational modes of methyl 2-pyridyl ketone oxime (mpko), the functional group common to all three systems.

- All three spectra also contain multiple peaks between 1570 cm^{-1} and 1600 cm^{-1} corresponding to C-O stretching in the different carboxylate anions and C-N stretching in the imine contained within the mpko ligand.

- The peak around 3100 cm^{-1} likely corresponds to aromatic C-H stretching (e.g. the C-H stretching vibrational mode in the naphthalene, anthracene, and pyrene ligands).